Space Weather

RESEARCH ARTICLE
10.1029/2025SW004730

Special Collection:
Coupling Processes from Space to Earth

# Forecasting Equatorial Plasma Bubbles From Precursor TEC Signatures Observed by C/NOFS

S. K. Das[1], C. Stolle[1], Y. Yamazaki[1], T. Yokoyama[2], M. Yamamoto[2], and S. Perwitasari[3]

[1]Leibniz Institute of Atmospheric Physics at the University of Rostock, Kühlungsborn, Germany, [2]Research Institute for Sustainable Humanosphere, Kyoto University, Kyoto, Japan, [3]National Institute of Information and Communications Technology, Koganei, Japan

**Abstract** This study investigates the potential of localized total electron content (TEC) perturbation measurements, possibly associated with bottomside upwelling of the F-layer, as precursors for forecasting ionospheric plasma irregularities, particularly the equatorial plasma bubbles (EPBs). We utilize TEC measurements from the Coherent Electromagnetic Radio Tomography (CERTO) onboard C/NOFS satellite, received by a GNU Radio Beacon Receiver (GRBR) at Phuket (8°N, 98.32°E; dip latitude ∼0.7°N) to identify early signatures of the F-layer upwelling in the evening sector, within the field-of-view of the Equatorial Atmosphere Radar (EAR) at Kototabang (0.2°S, 100.3°E, dip latitude ∼10°S). Simultaneous occurrences of EPBs are monitored using the scanning capability of EAR, enabling a direct comparison between the observed TEC perturbations and the development of EPBs. Additionally, ionosonde measurements from Chumphon (10.5°N, 99.4°E; dip latitude ∼3.6°N) are employed to substantiate these findings. The 445-day analysis (2012–2014) under varying solar and geomagnetic conditions shows that while TEC perturbations often precede EPBs, not all lead to their development. EPB occurrence has been found to vary with perturbation amplitude, inferring that only certain perturbation strengths are conducive to EPB formation. Further, a receiver operating characteristic (ROC) curve analysis indicates that a TEC perturbation threshold of 5.65% yields a prediction accuracy of ∼96%, providing a lead time of ∼18–86 min. These findings demonstrate the feasibility of a satellite-ground network comprising low-inclination satellites with GRBR-like receivers, sequentially traversing the same longitude sector at ∼30-min intervals, for real-time monitoring and forecasting of EPBs over a broad longitudinal sector.

**Plain Language Summary** Ionospheric plasma irregularities, such as the equatorial plasma bubbles (EPBs), disrupt satellite communication and navigation systems. Forecasting their day-to-day occurrence remains difficult due to complex growth and propagation characteristics. This study examines localized total electron content (TEC) perturbations, interpreted as potential signatures of bottomside F-layer upwellings, as precursor to EPB development. TEC measurements from the Communication/Navigation Outage Forecasting System (C/NOFS) satellite, received at a GNU Radio Beacon Receiver (GRBR) in Phuket, Thailand, are analyzed to identify potential early signatures of F-layer upwellings within the field-of-view of the Equatorial Atmosphere Radar (EAR) at Kototabang, Indonesia. Using EAR's scanning capability, these perturbations are directly compared with simultaneous EPB detections. Analysis of 445 days of observations under varying solar and geomagnetic conditions shows that the TEC perturbations often precede EPBs, though not all lead to their growth. A receiver operating characteristic (ROC) curve analysis indicates that a 5.65% TEC perturbation threshold yields ∼96% prediction accuracy with 18–86 min of lead time. These results highlight the feasibility of a satellite-ground observational network, using low-inclination satellites with GRBR-like receivers and ∼30-min longitudinal sampling, for real-time EPB monitoring and forecasting of EPBs over a large longitude sector.

**Key Points:**

- TEC measurements from C/NOFS are used to assess EPB prediction across a wide range of solar and geomagnetic conditions
- Early localized ionospheric perturbations, possibly linked to bottomside F-layer upwellings, were identified using C/NOFS TEC data
- Detection of localized TEC perturbations enabled EPB prediction with 96.40% accuracy

**Correspondence to:**
S. K. Das,
das@iap-kborn.de

**Citation:**
Das, S. K., Stolle, C., Yamazaki, Y., Yokoyama, T., Yamamoto, M., & Perwitasari, S. (2026). Forecasting Equatorial plasma bubbles from precursor TEC signatures observed by C/NOFS. *Space Weather*, *24*, e2025SW004730. https://doi.org/10.1029/2025SW004730

Received 21 SEP 2025
Accepted 20 DEC 2025

**Author Contributions:**
**Conceptualization:** S. K. Das
**Data curation:** S. K. Das, M. Yamamoto, S. Perwitasari
**Formal analysis:** S. K. Das
**Funding acquisition:** T. Yokoyama
**Investigation:** S. K. Das
**Methodology:** S. K. Das
**Resources:** S. K. Das
**Software:** S. K. Das, M. Yamamoto
**Supervision:** C. Stolle, Y. Yamazaki, T. Yokoyama
**Validation:** S. K. Das
**Visualization:** S. K. Das
**Writing – original draft:** S. K. Das
**Writing – review & editing:** S. K. Das, C. Stolle, Y. Yamazaki, T. Yokoyama



## 1. Introduction

Ionospheric plasma irregularities such as the equatorial plasma bubbles (EPBs) are plasma density irregularities with scale sizes ranging from a few centimeters to hundreds of kilometers that predominantly occur in the Earth's equatorial and low-latitude ionosphere during post-sunset hours (e.g., Abdu, 2001; Haerendel, 1973; Kelley, 2009). It was first observed in the form of diffused F-region echoes in an ionogram by Booker and Wells (1938) and termed as equatorial spread F (ESF). These irregularities can significantly disrupt radio wave propagation, satellite communications, and navigation systems, including causing Global Positioning System

(GPS) loss-of-lock (e.g., De Michelis et al., 2022; Kintner et al., 2007; Xiong et al., 2016), where satellite signals are lost due to signal degradation or disruption. As a result, EPBs can lead to inaccuracies in positioning and navigation services, particularly in critical applications like aviation and disaster management. The prediction of these events is essential for both scientific research and practical space weather applications to mitigate potential impacts on communication and navigation systems.

EPBs are believed to form after sunset at the base of the F layer near the magnetic equator through the Rayleigh-Taylor instability (RTI) mechanism, which arises under favorable background ionospheric conditions. Once initiated, these plume-like structures rise and expand latitudinally, producing wedges of plasma density depletions and irregularities across both hemispheres (e.g., Balsley et al., 1972; Kelley et al., 1976; Scannapieco & Ossakow, 1976; Sultan, 1996; Tsunoda et al., 1982; Weber et al., 1978; Woodman & La Hoz, 1976). A characteristic feature of EPBs is their eastward drift, driven by vertical electric fields produced by the F-region dynamos (e.g., Eccles, 1998; Haerendel et al., 1992). The growth rate of RTI is governed by several factors, such as zonal electric fields, neutral winds, the vertical gradient of F-region plasma densities, ion-neutral collision frequency, and magnetic field strength (e.g., Abdu, 2001; Burke et al., 2004; Kelley, 2009; Ott, 1978; Sultan, 1996). Additionally, previous studies have highlighted the importance of a seed perturbation primarily believed to be originated from atmospheric gravity waves (AGWs) in accelerating the growth of EPBs, leading to their rapid evolution and expansion (e.g., Kelley et al., 1981; Röttger, 1973; Tsunoda, 1985; Tsunoda et al., 1979; Woodman & La Hoz, 1976). These waves modulate the bottomside F-region plasma, creating a spatial wave structure with regions of enhanced and depleted electron density, which can trigger the RTI and lead to EPB formation from the depleted regions (e.g., Das et al., 2020, 2021; Huang & Kelley, 1996; Makela et al., 2010; Singh et al., 1997; Takahashi, 2008). Using ionosonde and radar observations Das et al. (2020) have demonstrated a close linkage between these pre-sunset wavestructures (zonal wavelength 160–520 km) with inter-bubble spacings of EPBs (zonal wavelength 200–550 km), inferring potential seeding mechanism for the formation of EPBs.

Numerous studies have investigated the relationship between the occurrence of EPBs and key ionospheric parameters, particularly the strength of the pre-reversal enhancement (PRE) of the zonal electric field and the height of the F-layer base. The PRE, which typically intensifies around sunset due to the combined action of the E- and F-region dynamos, plays a crucial role in initiating the RTI responsible for EPB formation (e.g., Clemesha & Wright, 1966). Similarly, a higher F-layer base altitude before sunset has been associated with increased EPB activity, likely due to enhanced instability growth conditions (e.g., Anderson & Redmon, 2017; Redmon et al., 2010). Specifically, limited success (~80%) has been achieved using threshold base height ($h'F$) of the F-layer (e.g., Anderson & Redmon, 2017) or with vertical drift associated to PRE (>40 m/s) obtained from Communications/Navigation Outage Forecasting System (C/NOFS) (Huang & Hairston, 2015) as an precursor to ESF. Besides, the field-line integrated growth-rate of the RTI, derived from key governing parameters of established models such as the Thermosphere-Ionosphere Electrodynamics General Circulation Model (TIEGCM) and the Ground-to-topside Model of Atmosphere and Ionosphere for Aeronomy (GAIA), has been employed to forecast EPB occurrence (Carter et al., 2014; Shinagawa et al., 2018). These models incorporate complex thermosphere–ionosphere interactions, including neutral wind dynamics, ionospheric conductivity, and geomagnetic activity. While this approach has demonstrated a prediction success rate of about 85% (Carter et al., 2014), its performance is still constrained by the intrinsic variability of the ionosphere and the limited spatial and temporal resolution of input parameters. Complementary to such model-based efforts, Das et al. (2021), using ionosonde and radar observations, showed that the local growth-rate of the RTI is strongly linked to the location of the EPB onset. Specifically, they found that events with growth-rates exceeding $1.0 \times 10^{-3}$ $s^{-1}$ are predominantly associated with freshly developed EPBs overhead (within $\pm 1°$ longitude of the ionosonde station), whereas lower growth-rates are typically linked to drifted or non-EPB events. Moreover, in recent years, numerical prediction approaches, particularly those based on machine learning (ML), have been increasingly applied to forecast EPB occurrence, achieving success rates of up to 75% (Garcia et al., 2023). Similarly, other ML-based methods (e.g., Reddy et al., 2023), as well as empirical models such as the Ionospheric Bubble Prediction (IBP) model (Stolle et al., 2024), have shown reliable performance in statistically predicting ionospheric plasma irregularities. Additionally, Hysell et al. (2019) reported that forecast models incorporating assimilated beacon data could be used to predict the locations of convective plume formation during ESF events.

Although the aforementioned methods offer reasonable capabilities in predicting the EPB occurrence, the inherent complexities in the spatio-temporal evolution, specifically the growth and zonal drift of EPBs, continue to pose significant challenges in predicting the day-to-day occurrence variability of EPBs (e.g., Das et al., 2021; Das, Janardana Reddy, et al., 2022). In this context, increasing attention has been directed toward the role of localized upwellings associated with large-scale wave structures (LSWS), which are superimposed on the PRE-driven uplift of the F-region bottomside before EPB development (e.g., Tsunoda, 2005; Tsunoda & Ecklund, 2007). In fact, direct observational evidence of LSWS was provided by the ARPA Long-Range Tracking and Instrumentation Radar (ALTAIR) at Kwajalein (e.g., Tsunoda, 1983; Tsunoda & White, 1981; Tsunoda et al., 1979), which revealed altitude modulations in electron density contours, characterized by zonal wavelengths of approximately 400 km, at the F-region bottomside. EPBs were observed to originate near the crests of these low-density regions, corresponding to localized upwellings. Evidence of LSWS preceding EPB/ESF development has also been reported in many studies (e.g., Singh et al., 1997; Thampi et al., 2009; Tulasi Ram et al., 2014). Besides, several studies have reported the satellite traces (STs), an ionogram signature linked to LSWS to be the precursor to the ESF (e.g., Narayanan et al., 2014; Tsunoda, 2008; Tsunoda et al., 2013). A working model on the hypothesis of LSWS followed by ESF/EPB development can be obtained at Tsunoda (2015). In a recent study, Patra and Das (2023) utilized ionosonde observations to demonstrate that the onset of EPB is strongly influenced by background ionospheric conditions, specifically characterized by the second temporal derivative of the F-layer base height, that is, $\frac{d^2h'F}{dt^2}$, which is indicative of localized bottomside F-layer upwelling. Their findings revealed that the predictive capability of $\frac{d^2h'F}{dt^2}$ as an EPB onset indicator is highly sensitive to the longitudinal proximity of the EPB initiation site relative to the ionosonde station. Reliable prediction was achieved when the onset occurred within approximately $\pm 1^\circ$ longitude of the ionosonde location. Building upon this approach, a subsequent study by Patra and Das (2025) demonstrated an exceptional post-sunset EPB prediction accuracy exceeding ~99% using ionosonde data from three geographically distributed stations across India.

Although this technique shows remarkable accuracy in predicting EPB onset near an ionosonde station, extending the prediction capability across a broader longitude sector can be resource-intensive and challenging. In this context, radio beacon measurements from the low-inclination low Earth Orbiting Satellites (LEOs) assume importance. LEOs have been widely utilized to investigate the ionospheric total electron content (TEC) using the dual-frequency differential phase technique (e.g., Aitchison & Weekes, 1959; Davies, 1980; Garriott, 1960). Although numerous polar-orbiting satellites carry beacon transmitters, C/NOFS with onboard Coherent Electromagnetic Radio Tomography (CERTO) beacon transmitter stands out as the first and only satellite placed in a near-equatorial orbit with a $\sim 13^\circ$ inclination. This unique capability allows C/NOFS to effectively observe and characterize zonal variations in TEC across equatorial and low-latitude regions. Interestingly, case studies have reported the occurrence of LSWS and their subsequent role in triggering EPB development, based on TEC measurements and scintillation observations from CERTO beacon signals onboard the C/NOFS satellite (e.g., Thampi et al., 2009; Tsunoda et al., 2013). In addition, the characteristics of LSWS preceding EPB formation have been extensively examined and reported in a comprehensive study by Tulasi Ram et al. (2014).

While previous studies have contributed significantly to our understanding of EPB development in association with LSWS, direct observational evidence, particularly in the spatial domain, linking localized upwellings to the subsequent formation of EPBs remains scarce. To address this gap, we investigate the linkage between localized TEC perturbations as a potential signature of localized upwelling derived from TEC measurements from CERTO beacon onboard the C/NOFS satellite, and the subsequent development of EPBs within the scanning field-of-view (FoV) of the Equatorial Atmospheric Radar (EAR) located at Kototabang ($0.2^\circ$S, $100.3^\circ$E, dip latitude $\sim 10^\circ$S). This investigation further aims to develop a predictive framework for EPB occurrence based on such localized precursors. The paper first outlines the methodologies used to detect the sites of potential localized upwellings and to determine EPB onset locations within the EAR's FoV. Subsequently, a series of representative case studies are presented to demonstrate the spatiotemporal evolution of EPBs following localized upwelling events. The predictive capability achieved through this analysis is then assessed, and the findings are discussed in the broader context of advancing future strategies for EPB prediction.

## 2. Methodology

### 2.1. Characterization of Potential Localized Upwellings (LSWS) From TEC Measurements

In this study, we investigate the zonal variation of TEC using measurements from the GNU Radio Beacon Receiver (GRBR) system (Yamamoto, 2008), installed at Phuket (8°N, 98.32°E; dip latitude ∼0.7°N). The GRBR system receives 150 and 400 MHz beacon transmissions from the C/NOFS satellite, which operates in a near-equatorial, low-inclination orbit. This configuration enables the examination of localized upwelling features associated with LSWS across the longitudinal sector of approximately 82°–114°E, encompassing the longitude of EAR at Kototabang.

For the present analysis, the line-of-sight TEC, derived from the C/NOFS-CERTO radio beacon signals, was converted to vertical TEC (VTEC) by assuming a mean ionospheric pierce point (IPP) height of 350 km. Due to the satellite's low-inclination orbit of ∼13°, its trajectory primarily spans longitudinal directions near the magnetic equator. As a result, the observed TEC variations along the satellite track mainly reflect longitudinal structures, with minimal influence from latitudinal changes. This configuration is particularly well-suited for studying longitudinal TEC patterns and equatorial ionospheric features.

To estimate absolute VTEC, the "single-station method" outlined in Tulasi Ram et al. (2012) is employed. This approach has been validated against the conventional two-station method (Leitinger et al., 1975) and ionosonde-derived TEC estimates. It accounts for the horizontal TEC gradients along the satellite track, which are primarily governed by longitudinal variations induced by local time effects. Under the assumption of a quasi-linear TEC distribution along the satellite path, an initial TEC offset is determined using a bisquare-weighted least squares fitting technique to improve estimation accuracy. To isolate spatially coherent signatures, large-scale TEC variations with zonal wavelengths exceeding 800 km are removed. The residual zonal perturbations in VTEC (in %) are interpreted as potential signatures of localized upwellings in the low-latitude ionosphere, consistent with the correspondence between the characteristics of the zonal TEC variations observed by C/NOFS and the bottomside upwelling structures detected in the ALTAIR incoherent scatter radar, as discussed in Tsunoda et al. (2011). Such longitudinal variations in the observed TEC perturbations may be associated with vertical plasma transport driven by zonally varying PRE linked to bottomside upwellings. This interpretation is consistent with the findings of Patra et al. (2025), who reported substantial differences in F-layer vertical drift velocities (approximately 29–49 m/s) within a short longitude zone and attributed this behavior to localized upwelling arising from spatially varying electrodynamics. It is therefore plausible that the zonal-scale negative TEC perturbations observed by C/NOFS reflect prevailing upwelling structures at the bottomside of the F layer. These perturbations are quantified in terms of relative fluctuations, expressed as $\Delta\mathrm{VTEC}/\mathrm{VTEC}$ (in %), computed as: $[\mathrm{VTEC}(t) - \langle\mathrm{VTEC}\rangle] \times 100/\langle\mathrm{VTEC}\rangle$, where $\mathrm{VTEC}(t)$ represents the instantaneous VTEC and $\langle\mathrm{VTEC}\rangle$ denotes the mean VTEC. More details on VTEC retrieval and LSWS extraction from C/NOFS beacon observation can be found in Tulasi Ram et al. (2012).

In this analysis, we characterized potential regions of localized upwellings by identifying the maximum TEC perturbation amplitudes observed by C/NOFS-CERTO within the EAR's FoV between 17:00 LT and the time of apex F-region sunset, considering that EPBs typically occur on or before the apex F-region sunset (e.g., Das, Pavanchaitanya, et al., 2022; Yokoyama et al., 2004). For context, the C/NOFS satellite operated in a low Earth elliptical orbit with a perigee of ∼400 km, an apogee of ∼850 km, and an orbital period of ∼97 min during the observed period. An example of a potential localized upwelling detected from GRBR-received TEC measurements can be obtained from Figure 3c.

### 2.2. Estimation of Onset Location of EPBs

To accurately determine the onset location of EPBs, this study utilizes the high-resolution scanning capability of the Equatorial Atmosphere Radar (EAR), operating at 47.0 MHz with a peak transmission power of 100 kW. The EAR is situated in Kototabang (0.2°S, 100.3°E, dip latitude ∼10°S), and is capable of detecting field-aligned irregularities (FAIs) associated with EPBs at spatial scales down to approximately 3 m. The radar employs an active phased-array antenna system that enables pulse-to-pulse electronic beam steering across a wide FoV, allowing for flexible and rapid scanning of the ionospheric volume (Fukao et al., 2003).

The EAR system scans a fan-shaped sector from 130° to 230° in azimuth, with beam zenith angles ranging from 24° to 37.5°, enabling observations of FAIs nearly perpendicular to the geomagnetic field over altitudes between

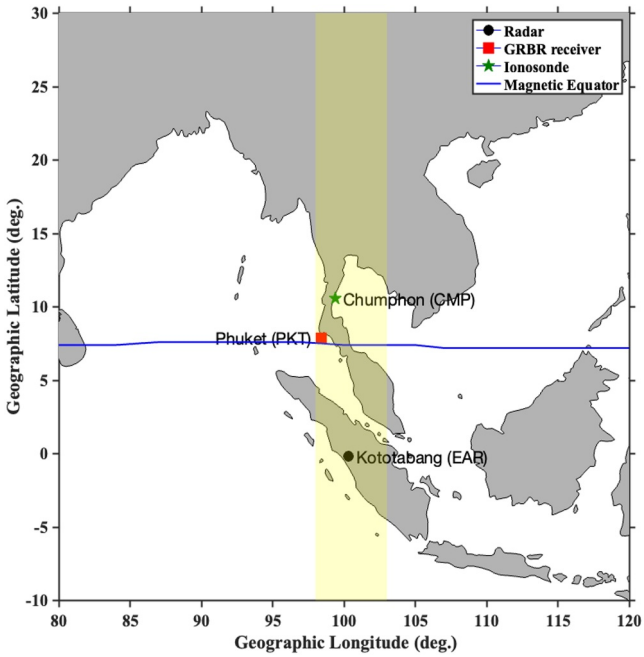


**Figure 1.** Map showing the geographic locations of the GRBR receiver in Phuket (PKT), the EAR radar in Kototabang (EAR), and the ionosonde station in Chumphon (CMP). The blue line marks the magnetic equator, while the shaded area (in yellow) represents the longitudinal observational coverage of EAR.

100 and 600 km. This capability is particularly advantageous for tracking the spatial distribution and zonal propagation of FAIs associated with EPBs. For the present analysis, EAR data were acquired at 16 azimuthal beam directions, covering a zonal distance of approximately ±500 km at an altitude of ∼400 km, centered over Kototabang. The multibeam observations were processed to derive the zonal distribution of radar echo signal-to-noise ratio (SNR), associated with FAIs. In the present study, EPB onset locations within the radar's scanning FoV are identified using the spatial distribution of SNR, following the approach outlined in Patra et al. (2014).

### 2.3. Characterization of Localized Upwelling Using Ionosonde Observation

To characterize localized bottomside upwellings in the ionosphere based on background ionospheric conditions, we employ ionosonde observations from Chumphon (10.5°N, 99.4°E; dip latitude ∼3.6°N), a station within the Southeast Asia Low-Latitude Ionospheric Network (SEALION) (Maruyama et al., 2007). The ionosonde is a Frequency Modulated–Continuous Wave (FM-CW) sounder operating in the 2–30 MHz range, providing ionograms every 5 min.

For the present analysis, the ionospheric parameter of interest is the virtual height of the F-layer base, denoted as $h'F$. To investigate localized vertical plasma upwelling over the ionosonde station, we strictly follow the methodology outlined in Patra and Das (2025). Specifically, the second temporal derivative of $h'F$, that is, $\frac{d^2h'F}{dt^2}$, is used as a diagnostic to detect upwelling events that precede the onset of an EPB. The first derivative $\frac{dh'F}{dt}$ is calculated and smoothed using a seven-point running mean (35-min window), from which the second derivative is subsequently computed. To reduce high-frequency fluctuations, the resulting $\frac{d^2h'F}{dt^2}$ series is further smoothed using a seven-point running mean. In accordance with Patra and Das (2025), a threshold of 0.01 m/s$^2$, observed between 17 LT till the apex F-region sunset, is used to characterize significant localized upwelling events.

It is noteworthy that the Chumphon ionosonde lies within ∼1° longitudinal distance of the EAR radar site and can therefore be used to characterize the background ionospheric conditions over EAR longitude (e.g., Patra & Das, 2023). For further details on the derivation and implementation of this technique, readers are referred to Patra and Das (2025).

### 2.4. Estimation of Growth-Rate of RTI ($\gamma$)

In order to substantiate the findings from TEC based observations, we have also estimated the local growth-rate of RTI following the methodology outlined in Das et al. (2021). Specifically, we adopted Equation (25) from Sultan (1996), which incorporates local parameters at the magnetic equator. Based on this formulation, the linear growth rate of the RTI is given as:

$$\gamma = \left(\frac{E}{B} - \frac{g}{\nu_{in}}\right)\frac{1}{n_0}\frac{\partial n}{\partial z} \quad (1)$$

where $\gamma$ is the growth-rate, $E$ is the zonal electric field, $B$ is the strength of the Earth's magnetic field, $g$ is the acceleration due to gravity, $\nu_{in}$ is the ion–neutral collision frequency, and $\frac{1}{n_0}\frac{\partial n}{\partial z}$ is the inverse vertical gradient scale length of the electron density. To calculate the gravity driven term that is, $\frac{g}{\nu_{in}}$, "g" is taken as 9.8 m/s$^2$, and to obtain the ion-neutral collision frequency ($\nu_{in}$) profile, we adopted the following equation from Kelley (2009):

$$\nu_{in} = 2.6 \times 10^{-9}(n_n + n_i)A^{\frac{1}{2}} \quad (2)$$

**Table 1**
*Details of Observational Data for Different Years With Yearly Averaged Solar Flux Condition, and Geomagnetic Activity in Terms of Kp*

| Year | Mean $F_{10.7}$ (sfu) | Mean Kp | Number of observations |
|---|---|---|---|
| 2012 | 121.2 | 1.70 | 130 |
| 2013 | 128.3 | 1.30 | 171 |
| 2014 | 145.1 | 1.47 | 144 |
| Total | | | **445** |

where, $n_n$ and $n_i$ are the neutral and ion density, respectively, and A is the mean neutral molecular weight. The altitude-dependent parameters of the aforementioned parameters are obtained from the MSISE-90 model (Hedin, 1991).

To evaluate the RTI growth-rate, we considered the time when the vertical drift of the F layer ($dh'F/dt$) reached its peak value during the evening hours, corresponding to the PRE period. The ion–neutral collision frequency ($\nu_{in}$) was calculated at the equatorial heights conjugate to the $h'F$ values observed by the Chumphon ionosonde at that time. The vertical drift term ($E/B$) was derived from the observed rate of change of $h'F$ ($dh'F/dt$) at Chumphon, assuming that $B$ is approximately horizontal over the magnetic equator. The inverse vertical gradient scale length, $\frac{1}{n_0}\frac{\partial n}{\partial z}$ is obtained from the electron density profile obtained from Chumphon's ionosonde.

Since this formulation does not account for field-line integrated parameters, the estimated $\gamma$ could be higher than the actual. It should also be noted that the estimated $\gamma$ at Chumphon longitude is considered representative for the EAR longitude as well, given that the zonal separation between the two locations is less than $\sim 1°$, consistent with Das et al. (2021).

It should be noted that the methods described in Sections 2.3 and 2.4 are not used for real-time forecasting of EPBs. Instead, they are used to substantiate the interpretations derived from the TEC-based measurements and to link the bottomside F-layer processes with those inferred from the TEC observations.

## 3. Observational Data Set and Geophysical Conditions

In this study, we analyze 445 days of data from 2012 to 2014, when C/NOFS beacon measurements within the EAR's longitudinal FoV, recorded by the GRBR receiver at Phuket (between 17 LT till the apex F-region sunset) and corresponding EAR radar observations were available on the same days. To supplement the primary data set and further validate the findings, ionosonde observations from Chumphon are also analyzed. The geographic locations of all stations involved in this study are presented in Figure 1. Table 1 summarizes the observational coverage of simultaneous EAR and beacon measurements for each year, including solar flux levels and geomagnetic activity characterized by the F10.7 index (Tapping, 2013) and the Kp index (Matzka et al., 2021), respectively.

Figure 2 summarizes the data distribution, where Panels 2a–2c present the distributions of day-of-year, solar flux, and geomagnetic activity, respectively. The data set spans a broad range of solar flux (F10.7 = 88–224 sfu) and geomagnetic conditions (Kp = 0–5.7), highlighting the inclusion of diverse geophysical conditions. Figure 2d presents a pie chart categorizing the 445 EAR observational days based on EPB activity: (a) EPB onsets detected within the EAR's FoV (in green), (b) EPBs that have onsets outside the FoV of EAR and drifted later in the FoV of EAR, during their eastward propagation (in sky-blue), and (c) cases with no EPB activity detected within the FoV (in gray). Additionally, the seasonal distribution of the data set is shown in Figure 2e, with classifications based on typical equinoctial and solstitial periods, namely, March equinox (February–April), June solstice (May–July), September equinox (August–October), and December solstice (November–January).

## 4. Results

### 4.1. EPB Onset Overhead to EAR Longitude

Figure 3 shows a case study on 28 March 2013, highlighting a freshly developed EPB event observed over the EAR longitude. Figure 3a illustrates the trajectory of the IPPs corresponding to the beacon signals transmitted by C/NOFS and received by the GRBR receiver at Phuket along its orbit at 12:05 UT. Figure 3b shows the variation in the estimated VTEC, and Figure 3c represents the TEC perturbations (in %) along the IPP longitude. A pronounced TEC perturbation exceeding 25% (negative $\Delta VTEC/VTEC$) can be observed between 105 and 110°E, outside the EAR's FoV. Additionally, a second perturbation, with an amplitude of ∼10%, can be observed shortly after the E-region sunset (green dashed line) at 99–101°E (right above the EAR longitude), within the EAR's FoV (yellow shaded region). Note that the ∼10% TEC perturbation is evident over the EAR longitude (Kototabang) around 18:40 LT.

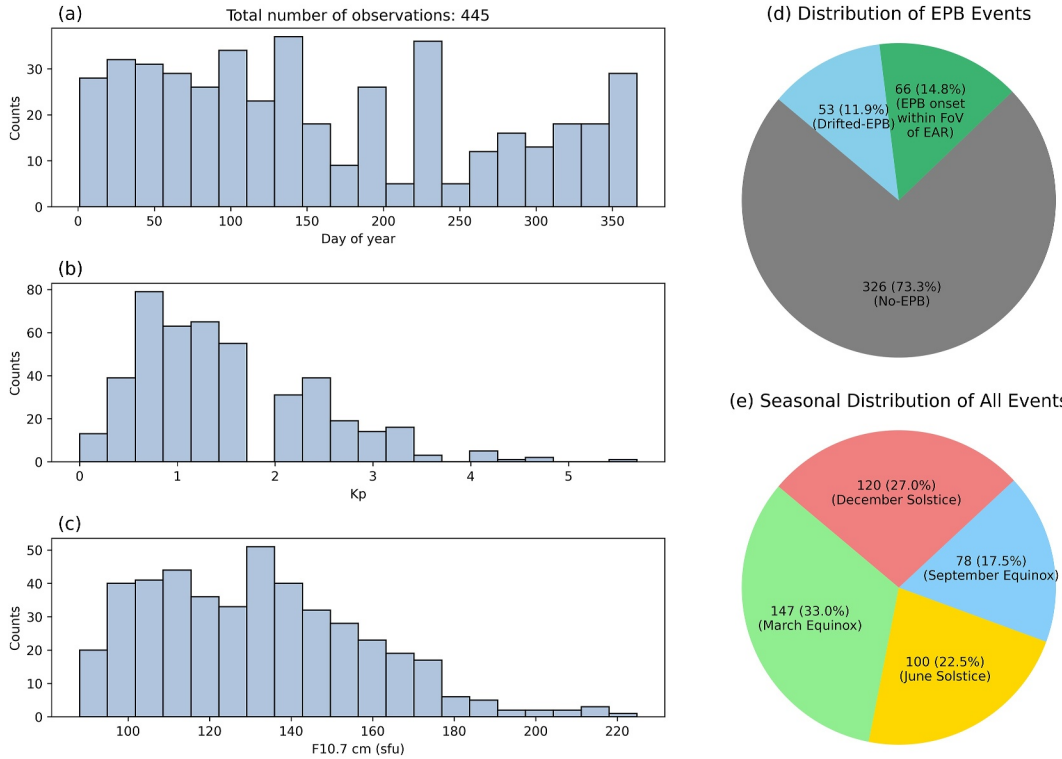


**Figure 2.** Distribution of the observational data set (445 days) in terms of (a) day-of-year, (b) geomagnetic index (Kp), and (c) solar-flux level (F10.7cm). Pie-charts showing (d) distribution of observations with EPBs onset within the field-of-view (FoV) of EAR, drifted EPBs, and no-EPBs and (e) seasonal distribution of the observational data set.

Figures 3d–3f show the ionosonde observation from Chumphon on the same day. The top panel shows the temporal variation of $h'F$ from 14 LT until the start of the ESF in the ionogram (represented as gray vertical lines), where the $h'F$ can be seen to attain a peak height of ∼360 km. The middle panel show the temporal variation of the vertical drift of the F-layer bottom $\left(\frac{dh'F}{dt}\right)$, which can be seen to attain a maximum of ∼40 m/s prior to the ESF onset. Similarly, the second time derivative of the F-layer bottom height $\left(\frac{d^2h'F}{dt^2}\right)$ exceeds 0.01 m/s$^2$ prior to the appearance of ESF in the ionogram, indicating prevailing bottomside F-layer upwelling over the EAR longitude and suggesting the imminent onset of an overhead EPB. This inference aligns with the findings of Patra and Das (2023, 2025), where a threshold of $\frac{d^2h'F}{dt^2} > 0.01$ m/s$^2$ was used to predict overhead EPB onset. Furthermore, the RTI growth rate ($\gamma$), estimated following the methodology described in Section 2.4, is found to be $12.32 \times 10^{-4}$ s$^{-1}$, reinforcing the evidence of a fresh EPB onset above the ionosonde station (Das et al., 2021) and consistent with the $\frac{d^2h'F}{dt^2}$ diagnostic.

Figures 3g and 3h shows the EAR observation on the same evening between 18 and 06 LT (next day). The top panel shows the Altitude-Time-Intensity (ATI) map of the signal-to-noise ratio (SNR) of FAIs observed by an antenna beam looking southward and perpendicular to magnetic field lines, whereas the bottom panel shows the temporal variation of echo intensity from EPB plumes against zonal distance at an altitude of 300 km. The ATI map confirms the presence of two backscatter plumes of EPBs, both extending more than 500 km in the FoV of EAR on this evening. The bottom panel reveals that while the first EPB plume has originated right overhead of EAR longitude at ∼19:42 LT and drifted eastward afterward, the second EPB has occurred at western longitude outside the radar's FoV and drifted over EAR later during the evening (at ∼21:25 LT).

This observation confirms the presence of a deep TEC perturbation (∼10%) preceding the onset of a fresh EPB over the EAR longitude by approximately 1 hr, while simultaneous ionosonde measurements from Chumphon provide evidence of a prevailing upwelling structure at the bottomside of the F-layer.

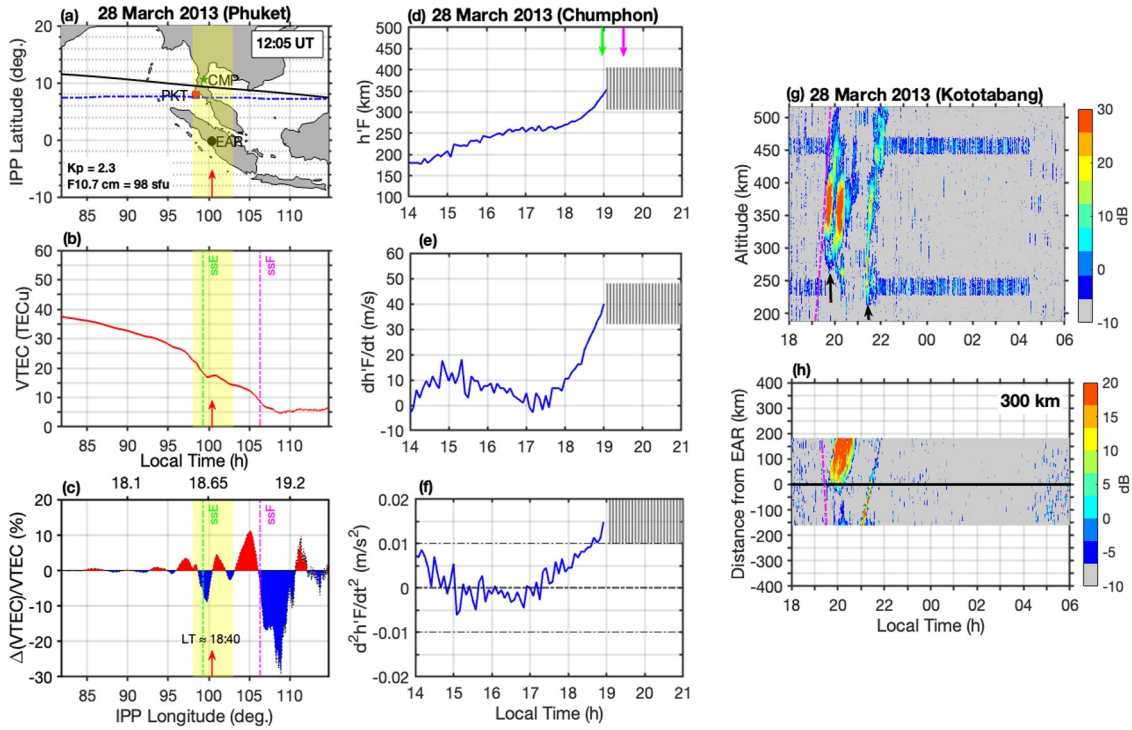


**Figure 3.** (a) Trajectory of the IPPs (in solid black) corresponding to the beacon signals transmitted by C/NOFS and received by the GRBR receiver along its orbit at 12:05 UT, (b) vertical TEC, and (c) TEC perturbation along IPP longitude. The red vertical arrow depicts the location of Kotatabang (EAR). The dashed vertical lines in green and magenta colors in panels (b) and (c) represent the E- and F-region sunset terminators, respectively. Temporal variations in (d) $h'F$, (e) $\frac{dh'F}{dt}$, and (f) $\frac{d^2h'F}{dt^2}$ observed by ionosonde at Chumphon. The green and magenta down arrows represent the E- and F-region sunset times over Chumphon. (g) Altitude-time variations of the signal-to-noise ratio (SNR) of field-aligned irregularities (FAIs), and (h) Zonal distribution and movement of FAIs at 300 km, observed by EAR on 28 March 2013. The dashed-dotted blue line in panel (a) represents the magnetic equator. The dashed magenta line in (g) and (h) represents the sunset times at different altitudes and 300 km, respectively. The black vertical arrows in (g) mark the times of the occurrence of FAIs associated with EPBs.

### 4.2. EPB Onset Slightly East of EAR Longitude

Figure 4 depicts a case study on 04 April 2012, where the onset of the EPB occurred slightly east of EAR longitude but within the radar's FoV. Figure 4a shows the trajectory of the IPPs of the beacon rays transmitted by C/NOFS and received at GRBR receiver along its orbit at 11:59 UT. Figure 4b shows the variation of the estimated VTEC along the IPP trajectory between 81 and 114°E. From Figure 4c, a large TEC perturbation, exceeding 30% with respect to the background TEC, can be observed within EAR's FoV at 101–103°E around ∼18:44 LT, right after the E-region sunset.

Figures 4d–4f present ionosonde observations from Chumphon on the same day, spanning from 14 LT until the onset of ESF as indicated in the ionograms. The virtual height of the F-layer ($h'F$) can be seen to reach a maximum of ∼320 km near the local sunset and remains relatively stable around this altitude until 20:30 LT (Figure 4d). Figure 4e shows that the peak vertical drift velocity of the F-layer $\left(\frac{dh'F}{dt}\right)$ reaches a maximum of ∼10 m/s around the local sunset and declines sharply thereafter. Notably, the vertical acceleration $\left(\frac{d^2h'F}{dt^2}\right)$ peaks at approximately 0.004 m/s$^2$ near 18 LT and decreases afterward, as can be noted in Figure 4f. These observations strongly indicate the absence of a prevailing bottomside upwelling over Chumphon/EAR longitude and overhead EPB onset on this evening, consistent with Patra and Das (2023, 2025). It is important to note that the zonal separation between the ionosonde at Chumphon (99.4°E) and the longitude of the detected TEC perturbation exceeds ∼2°. Given that the ionosonde's sensitivity to characterize the background ionospheric conditions is generally limited to approximately ±1° longitude from the station (e.g., Patra & Das, 2023, 2025), the observed peak $\frac{d^2h'F}{dt^2}$ of 0.004 m/s$^2$ suggests conditions favorable for either no fresh EPB onset or their lateral drift over Chumphon/EAR longitude later during the evening. Furthermore, the estimated RTI growth-rate ($\gamma = 5.02 \times 10^{-4}$ s$^{-1}$) supports this interpretation, suggested by the $\frac{d^2h'F}{dt^2}$ analysis (Das et al., 2021).

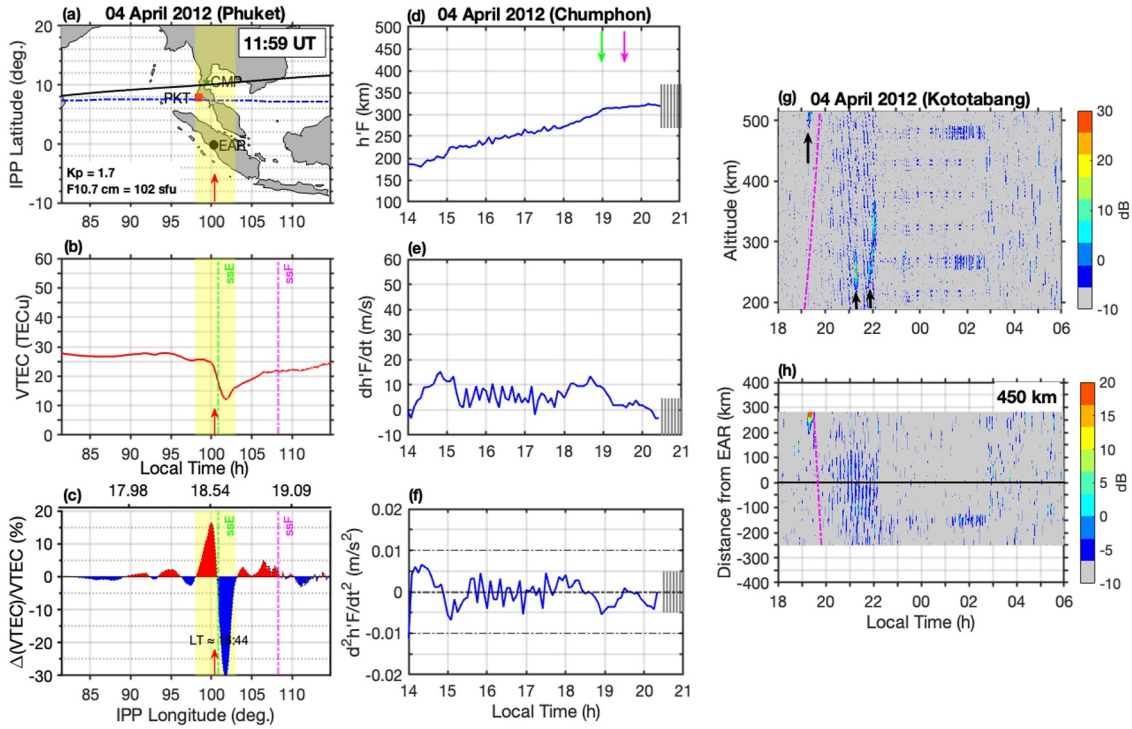


**Figure 4.** Same as Figure 3. But on 04 April 2012.

Figures 4g and 4h show the ATI and zonal distribution maps of FAIs as observed by EAR on the same evening. The top panel (Figure 4g) illustrates the presence of three distinct backscatter EPB plumes at ∼19:20, 21:18, and 21:48 LTs. The map depicting zonal distribution of FAIs at 450 km, shown in Figure 4h, reveals that the first EPB has originated slightly east (∼210 km) of Kototabang at 19:24 LT (longitude specific) and subsequently drifted eastward, while the other two plumes have developed outside FoV of EAR (westward) and drifted at later local time (not detected here, due to limited height of the EPB plumes).

This observation clearly demonstrates that, while the beacon data from C/NOFS captured early signatures of localized upwelling slightly east of Kototabang, approximately 40 min before EPB onset, the ionosonde at Chumphon was unable to characterize this localized upwelling due to its limited capability in characterizing the background ionospheric conditions at locations distant from the station.

### 4.3. EPB Onset West of EAR Longitude

Figure 5 shows another case study on 23 February 2014, where an EPB onset took place at a western longitude, outside the EAR's FoV, and subsequently appeared later in the evening as it propagated eastward. Figure 5a displays the trajectory of the IPPs corresponding to the beacon signals transmitted by C/NOFS and received at the GRBR receiver at 12:17 UT. Although the estimated VTEC from the beacon measurements does not show any large variation with the IPP longitude (Figure 5b), a TEC perturbation of maximum amplitude of ∼3% can be observed post E-region sunset within the FoV of EAR (in Figure 5c).

Figure 5d presents the temporal evolution of the bottomside F-layer height ($h'F$), derived from ionosonde observations at Chumphon, spanning 14 LT till 21 LT (ESF appears in the subsequent ionograms). The altitude increases steadily and reaches a maximum of ∼400 km around 20 LT. The corresponding vertical drift $\left(\frac{dh'F}{dt}\right)$ peaks at ∼30 m/s around the local sunset (Figure 5e). The vertical acceleration $\left(\frac{d^2h'F}{dt^2}\right)$ attains a maximum of 0.008 m/s$^2$ around 18:30 LT (Figure 5f), indicative of conditions that favor either the absence of an overhead EPB onset or their lateral drift over Chumphon/EAR longitude later in the evening (Patra & Das, 2023, 2025). The estimated RTI growth-rate ($\gamma = 8.94 \times 10^{-4}$ s$^{-1}$) further supports this interpretation of a drifting or no-EPB scenario over the EAR longitude (Das et al., 2021).

10.1029/2025SW004730

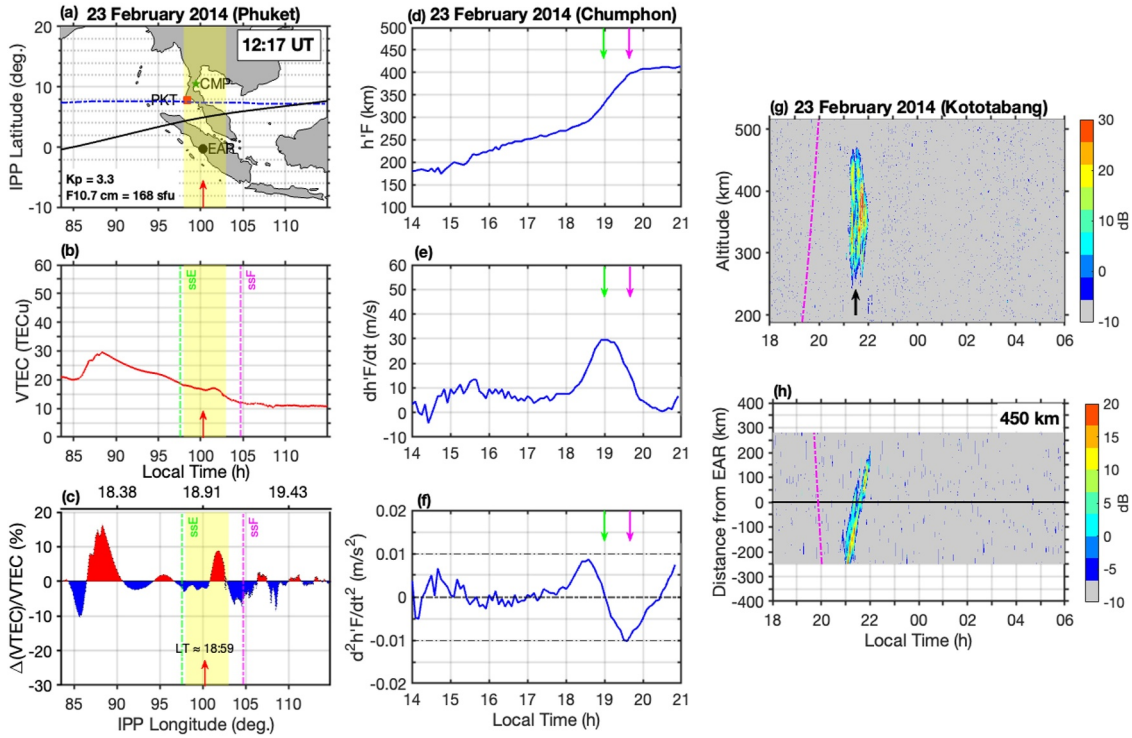


**Figure 5.** Same as Figure 3. But on 23 February 2014.

The ATI map from EAR (Figure 5g) reveals the presence of a strong backscatter EPB plume around ∼21 LT over the radar site. The zonal distribution of echo SNR at 450 km altitude in Figure 5h indicates that the EPB has originated west of the EAR's FoV and subsequently drifted eastward into the radar's FoV, initially appearing near the westernmost beam.

This case study clearly demonstrates that a small TEC perturbation (∼3%) did not lead to an overhead fresh EPB onset. This is also consistent with the ionosonde measurements from Chumphon, suggesting conditions unfavorable for overhead EPB development or indicative of a drifting EPB event.

### 4.4. No-EPB Onset Within the Field-of-View of EAR

Figure 6 presents a case study from 30 March 2013, during which no EPB occurrence was observed throughout the evening within the FoV of EAR. Figure 6a displays the trajectory of the IPPs corresponding to the beacon signals transmitted by C/NOFS and received by the GRBR receiver along its orbit at 11:57 UT. As illustrated in Figure 6b, the longitudinal variation of VTEC along the IPP does not exhibit any significant fluctuations within the EAR's FoV. This is further supported by the VTEC perturbation shown in Figure 6c, where negligible or very small perturbation amplitudes are observed within the EAR's FoV.

Ionosonde observations from Chumphon, shown in Figure 6d, indicate that the bottomside F-layer height ($h'F$) reached a maximum altitude of ∼300 km near local sunset. The corresponding vertical drift $\left(\frac{dh'F}{dt}\right)$ attained a peak value of ∼10 m/s (Figure 6e). Further, the vertical acceleration $\left(\frac{d^2h'F}{dt^2}\right)$ reached a maximum of 0.002 m/s$^2$ around 18:10 LT (Figure 6f), suggesting conditions favorable for either the absence of an overhead EPB onset or lateral drift of EPBs over Chumphon/EAR longitude (e.g., Patra & Das, 2023, 2025). In addition, an estimated RTI growth rate ($\gamma$) of $4.43 \times 10^{-4}$ s$^{-1}$ further supports the drifting or no-EPB scenario over Chumphon/EAR longitude (Das et al., 2021).

The ATI map from EAR (Figure 6g) shows no evidence of EPB occurrence during this evening. This agrees with the observed negligible TEC perturbations over EAR longitude and ionosonde measurements from Chumphon,

10.1029/2025SW004730

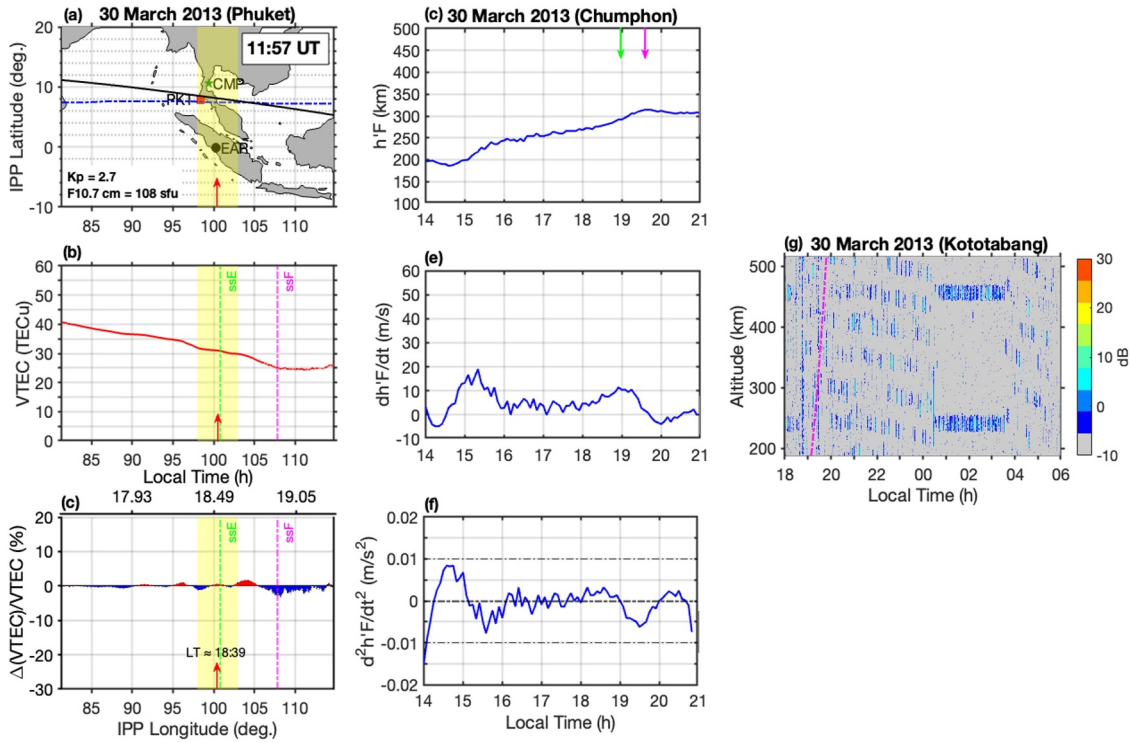


**Figure 6.** Same as Figure 3. But on 30 March 2013 (without the zonal distribution map of FAIs at a fixed altitude).

which indicate conditions favorable for either absence of an overhead EPB onset or drifting-EPB occurrence, later during the evening.

### 4.5. Post-Midnight EPB Onset Overhead to EAR Longitude

Although the present analysis primarily focuses on characterizing localized upwellings from TEC observations preceding post-sunset EPB onset, here we present a case study from 05 July 2012, the only case in which an EPB onset was observed near local midnight within EAR's FoV. Notably, this is the only instance of a fresh midnight EPB onset detected within the radar's FoV during the entire observation period, with concurrent measurements of TEC data from CNOFS's beacon received at GRBR and EAR observations.

Figure 7a displays the trajectory of the IPPs corresponding to the beacon signals transmitted by C/NOFS and received by the GRBR receiver along its orbit at 14:35 UT. As can be seen from Figure 7b, the estimated VTEC exhibits distinct longitudinal variability, with prominent modulation near 100°E. The corresponding TEC perturbation profile along the IPP (Figure 7c) reveals significant depletion, exceeding ∼15% over the EAR longitude, along with a secondary perturbation of ∼10% near 107°E (outside EAR's FoV). The TEC perturbation over EAR is observed at 21:16 LT, well after the local F-region sunset. Notably, ionosonde observations from Chumphon cannot be shown for this event, as no data were available on that evening.

The ATI map from EAR, shown in Figure 7d, displays a strong backscatter EPB plume around local midnight (00 LT), along with two smaller plumes observed near ∼23 LT and ∼03 LT, respectively. The spatial distribution of FAIs at 300 km altitude, shown in Figure 7e, depicts that the onset of the first EPB plume occurred overhead to EAR longitude at ∼23 LT. In contrast, the other two EPB plumes (observed at ∼00 LT and ∼03 LT) appear to have originated outside the EAR's FoV (westward) and subsequently drifted in later during the night.

## 5. Optimization of TEC Perturbation Threshold Using ROC Analysis

Figure 8a shows the histogram of the maximum TEC perturbation amplitudes (in %), observed by C/NOFS during its passage over EAR's FoV for the observation period. Events with EPB onset within the EAR's FoV are shown in green (excluding the post-midnight EPB event on 05 July 2012), while gray bars represent cases with either

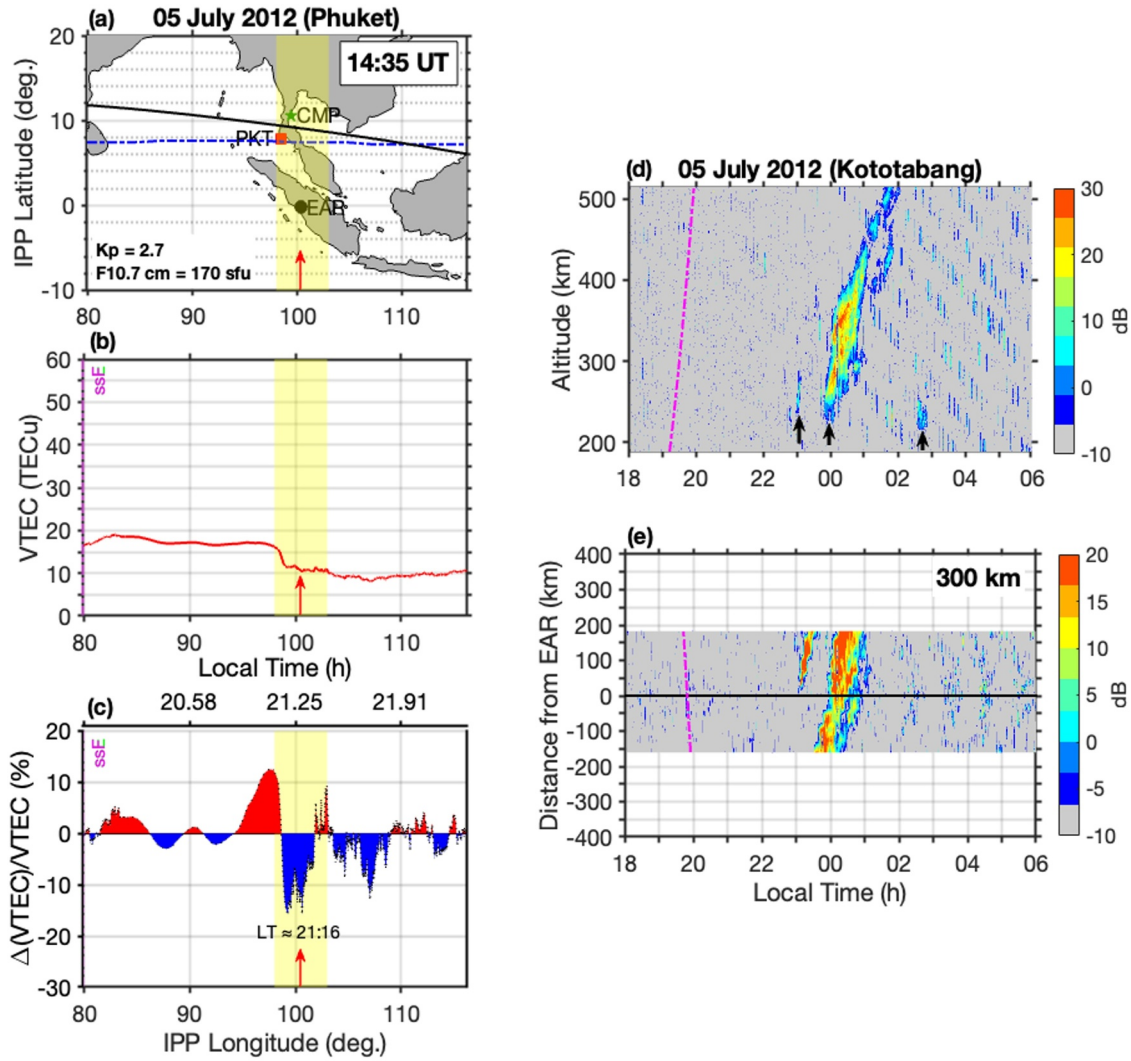


**Figure 7.** Same as Figure 3. But on 05 July 2012 (excluding the ionosonde observation from Chumphon).

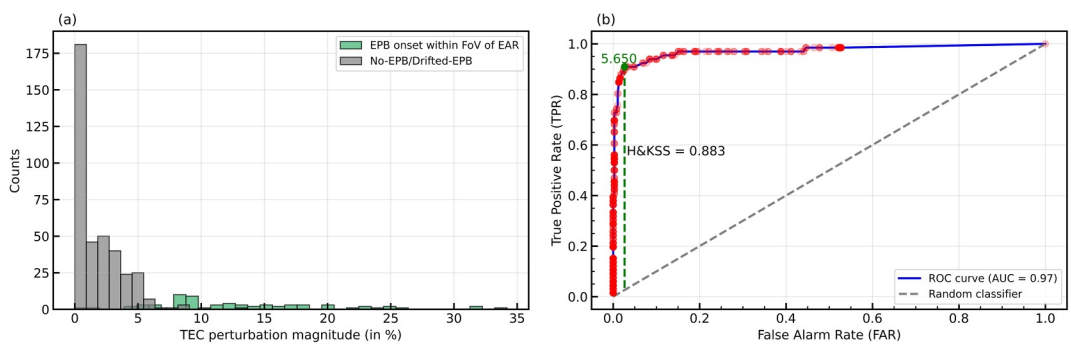


**Figure 8.** (a) Histogram of TEC perturbation amplitudes (in %) for events with EPB onset within the field-of-view (FoV) of EAR (green) and for No-EPB/Drifted-EPB cases (gray). (b) The receiver operating characteristic (ROC) plot depicting the probability of detection as a function of the false alarm rate (FAR) by varying the threshold of TEC perturbation amplitude above which an EPB onset within the EAR's FoV is forecasted. The optimal TEC threshold is obtained at $T_h = 5.65\%$ where H&KSS maximizes with a value of 0.883, shown as a dashed line in green color. The gray dashed line represents the random classifier line of the ROC plot.

**Table 2**
*2 × 2 Contingency Table Showing the Relationship Between Radar-Confirmed EPB Occurrences and Binary Forecasts Generated by Thresholding TEC Perturbation Amplitudes*

| | Forecast using TEC perturbation | | |
|---|---|---|---|
| EAR observation | Yes | No | Total |
| Event | True Positive (TP) | False Negative (FN) | TP + FN |
| Non-event | False Positive (FP) | True Negative (TN) | FP + TN |
| Total | TP + FP | FN + TN | N = TP + FP + FN + TN |

*Note*. Event = Events with EPB onset within EAR's FoV; Non-event = No-EPB/Drifted EPB events.

no-EPB or drifted EPB events. Note that the TEC perturbation amplitudes span a wide range from 0% to ∼34%, and importantly, there exists an overlapping region where both EPB and non-EPB/drifting-EPB events are present. This overlap introduces uncertainty in selecting a reliable TEC threshold for predicting EPB onset. To address this, a receiver operating characteristic (ROC) curve analysis is conducted to systematically evaluate the prediction performance and determine an optimal threshold value. This method is widely used to evaluate the performance of probabilistic classifiers and has been effectively applied to space weather forecasting models (e.g., Barnes et al., 2016; Murray et al., 2017; Nishizuka et al., 2020). In this context, each TEC perturbation value is treated as a probabilistic score, and predictions are assessed against EPB onset within EAR's FoV (ground truth) over a range of thresholds. For each threshold, the outcomes are classified into true positives (TP), false positives (FP), true negatives (TN), and false negatives (FN). These categorizations can be easily understood from the contingency table provided in Table 2.

The ROC curve illustrates the relationship between the true positive rate (TPR) and the false alarm rate (FAR) across a range of threshold values (e.g., Mason, 1982; Swets, 1973). Based on the contingency table constructed from TEC perturbation–based forecasts and radar-confirmed EPB occurrences, the TPR and FAR are defined as follows (e.g., Mason, 1982).

$$TPR = \frac{TP}{TP + FN} \quad and \quad FAR = \frac{FP}{FP + TN} \tag{3}$$

To evaluate the performance of EPB occurrence prediction based on TEC perturbation amplitudes, a ROC curve is constructed by examining how the binary classification of events changes with varying threshold values. Here, the TEC perturbation amplitude (in %) is treated as a predictive parameter, and binary outcomes are determined by applying a threshold value $P_{\text{th}}$. If the perturbation amplitude exceeds $P_{\text{th}}$, the event is classified as an EPB occurrence (event); otherwise, it is classified as a non-occurrence (non-event). By systematically varying $P_{\text{th}}$ across its full range, a series of contingency tables can be generated. From each table, the TPR and FAR can be computed, enabling the construction of the ROC curve for evaluating predictive performance. Plotting TPR against FAR for all thresholds yields the ROC curve. This curve illustrates the trade-off between correctly detecting EPB events and the rate of false alarms. A ROC curve that lies above the diagonal reference line (the 45° line from (0,0) to (1,1)) indicates skill in the prediction system, whereas a curve that follows this diagonal suggests no discriminative ability (i.e., a no-skill forecast). In the ideal case of perfect prediction, the ROC curve would pass through the points (0,0), (0,1), and (1,1), indicating a TPR of 1 and a FAR of 0.

The overall effectiveness of the binary classifier can be quantified using skill scores derived from the ROC curve. One such measure is the ROC Skill Score (ROCSS), also referred to as the Gini coefficient $G_c$ (e.g., Jolliffe & Stephenson, 2011), calculated as $G_c = 2A–1$, where A is the area under the ROC curve (AUC). A $G_c$ value of 1 represents a perfect classifier, while a value of 0 corresponds to no skill. To identify the optimal threshold, we computed the Hanssen and Kuipers Skill Score (H&KSS), also known as the True Skill Statistic (TSS), which measures the ability of a forecast to distinguish between events and non-events, independent of how often they occur (e.g., Hanssen & Kuipers, 1965). It is defined as the difference between the TPR and FAR:

$$\text{H\&KSS} = \text{TPR} - \text{FAR} \tag{4}$$

**Table 3**
*Summary of EPB Occurrence Prediction Using a TEC Perturbation Threshold of 5.65%*

| Year | Prediction for EPB onset within FoV of EAR | Prediction for no-EPB onset within FoV of EAR | EPB onset observed within FoV of EAR | No-EPB/Drifted-EPB observed within FoV of EAR |
|---|---|---|---|---|
| 2012 | 24 | 106 | 21 | 109 |
| 2013 | 17 | 154 | 16 | 155 |
| 2014 | 29 | 115 | 29 | 115 |

The score ranges from −1 to +1, where +1 indicates perfect skill, 0 represents no-skill (random guessing), and negative values indicate poor performance. Because it accounts for both correct detections and false alarms, H&KSS provides a statistically sound and reproducible method for the threshold selection in TEC-based EPB forecasting.

We analyze 445 days of data collected during 2012–2014, during which simultaneous TEC measurements from C/NOFS' beacon, recorded at GRBR and EAR observations were available (see Table 1 for details), for the ROC analysis. A step size of 0.25% in perturbation amplitude is used to construct the contingency table (see Table 2) based on precursor TEC perturbations observed by the C/NOFS beacon. Figure 8 represents the resulting ROC curve, constructed from this threshold sweep. The ROC analysis reveals a high predictive performance, with an AUC of 0.96 and $G_c$ of 0.94, indicating excellent classification skill. The optimal threshold of TEC perturbation amplitude $(T_h)$ is determined to be 5.65%, corresponding to the H&KSS score of 0.883. This threshold represents the point at which the balance between the TPR and FPR is optimized, providing the most effective criterion for EPB prediction using precursor TEC perturbations, based on the present analysis.

## 6. Prediction of EPB Occurrence Using Optimized TEC Perturbation Threshold

To evaluate the predictive capability of EPBs using precursor TEC perturbations as an indicator, a threshold amplitude of 5.65%, determined from ROC analysis, is applied. The statistics show that out of 445 events, EPB onsets within EAR's FoV were predicted in 70 cases and non-formation of EPB/drifted EPB events (within the EAR's FoV) were predicted in 375 cases. Observational statistics reveal that the EPB onsets within the EAR's FoV were recorded in 66 cases, whereas 379 cases corresponded to either no-EPB occurrence or drifted-EPBs. A year-wise summary of predicted and observed EPB occurrences is provided in Table 3. With respect to the prediction performance, out of a total of 445 events, the statistics can be summarized as follows: 60 cases of true positive (TP), corresponding to instances where EPB onset occurred within the FoV of EAR; 369 cases of true negative (TN), which include no-EPB and drifted-EPB events (when EPB onset occurred west of the FoV of EAR and drifted into EAR's FoV later during the night); 6 cases of false negative (FN), where EPB onset occurred within EAR's FoV but the precursor TEC perturbation amplitude detected were less than 5.65%; and 10 cases of false positive (FP), where the detected TEC perturbation amplitude were greater than 5.65% but no-EPB/drifted EPB events were noticed within the FoV of EAR. Figure 9 illustrates the statistics of prediction and occurrence of EPB onset within the FoV of EAR in the form of a quadrature chart. The positive (negative) *X*-axis represents prediction for EPB onset (non-formation of EPB) within the FoV of EAR, and the positive (negative) *Y*-axis represents observation of EPB onset (no-EPB onset or drifted EPB) within EAR's FoV. This figure clearly demonstrates that we successfully predicted the occurrence of 60 EPBs out of 70 cases, with 10 missed cases where EPB onset did not occur despite the TEC perturbation amplitudes were greater than 5.65%. To assess the effectiveness of the prediction technique, we calculated the prediction accuracy (in %) as

$$\text{Accuracy} = \frac{TP + TN}{TP + TN + FP + FN} \tag{5}$$

which yields 96.40%.

Similarly, we have also evaluated the prediction capability of the EPB occurrence for different seasons, which are shown in Figures 10a–10d. The observed accuracy of prediction for different seasons can be summarized as: 95.24% for the March equinox, 96% for the June solstice, 97.44% for the September equinox, and 97.50% for the December solstice.

10.1029/2025SW004730

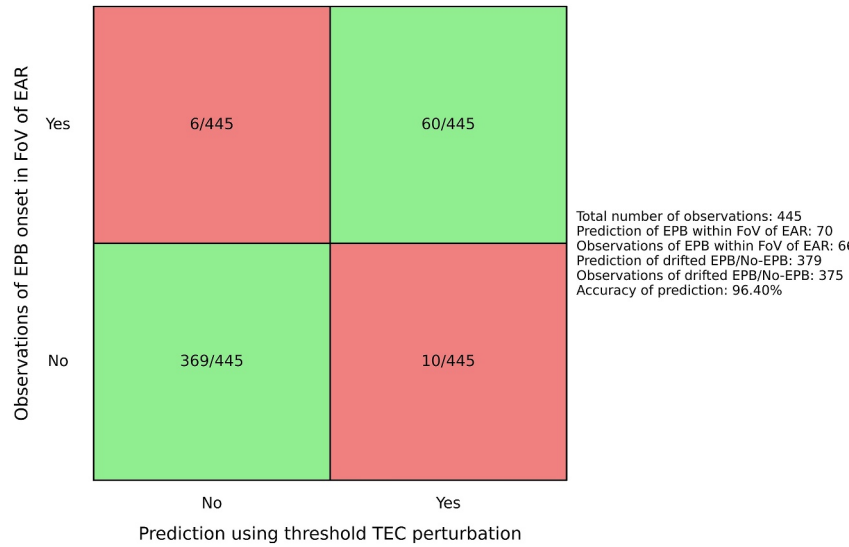


**Figure 9.** Quadrature chart showing statistics of prediction and onset of EPBs within the EAR's FoV. Positive (negative) *X*-axis represents prediction for the onset of EPB within FoV of EAR (no-EPB/drifted-EPB events within FoV of EAR) and positive (negative) *Y*-axis represents the observation of EPB onset (no-EPB/drifted EPB events) within FoV of EAR.

## 7. Discussion and Way Forward

This study demonstrates a high predictive capability for EPB occurrences, achieving an overall success rate of ∼96.4% with seasonal prediction accuracy of ∼95%, ∼96%, ∼97%, and ∼97.5% for March equinox, June solstice, September equinox, and December solstice, respectively, through the identification of potential early signatures of localized ionospheric upwellings using TEC perturbations derived from C/NOFS beacon transmissions received at a GRBR ground station (Phuket). The analysis is based on a substantial data set covering 445 days during 2012–2014, encompassing a broad range of solar flux levels and geomagnetic activity conditions (see Figure 2). Importantly, the proposed approach also demonstrates predictive capability for less frequent events, such as post-midnight EPB occurrences, exemplified by the case study on 05 July 2012 (see Figure 7), when an effective threshold TEC perturbation amplitude of 5.65% is applied. Nonetheless, we acknowledge that a more comprehensive analysis involving a larger data set encompassing freshly developed post-midnight EPBs within the EAR's FoV is necessary to enhance the reliability of such predictions. Focusing on a subset of 60 events where EPB onset were successfully predicted using a threshold TEC perturbation amplitude of 5.65%, we examine the lead time between the detection of the precursor TEC signature and the actual occurrence of EPBs. Figure 11a presents a scatter plot comparing the local times of detection of potential signatures of localized upwellings using a threshold TEC perturbation amplitude of 5.65% ($LT_{TEC}$) and the local time of EPB onset within the EAR's FoV ($LT_{EAR}$). This analysis considers only post-sunset EPB events and excludes the isolated post-midnight event on 05 July 2012. The threshold TEC perturbations were detected between 18:12 LT and 19:30 LT, whereas EPB onsets were recorded between 19:12 and 20:12 LT. It is noteworthy that in certain instances, the potential localized upwelling structures, characterized by the threshold TEC perturbation amplitude, were detected well before the E-region sunset, consistent with findings reported in earlier studies (e.g., Thampi et al., 2009). The lead time distribution shown in Figure 11b, defined as the time difference between EPB onset and detection of threshold TEC perturbation, that is, $LT_{EAR} - LT_{TEC}$, ranges from approximately 18 min to as high as 86 min, with a peak around 40 min. This indicates that, typically, EPBs are observed around 40 min after the initial detection of significant TEC perturbations. However, it is important to recognize that the lead time is influenced by the orbital characteristics of the satellite; in the case of C/NOFS, the orbital period is approximately 97 min (e.g., de La Beaujardière et al., 2004).

We also present the comparative analysis of characterizing localize upwelling signatures using temporal variation of $\frac{d^2 h'F}{dt^2}$ (Patra & Das, 2025) and growth-rate analyses (Das et al., 2021) from an ionosonde located at Chumphon and spatial measurements of TEC data from CERTO-beacon onboard C/NOFS. Results clearly reveal that although an ionosonde is capable of detecting localized upwelling within a very close proximity around the

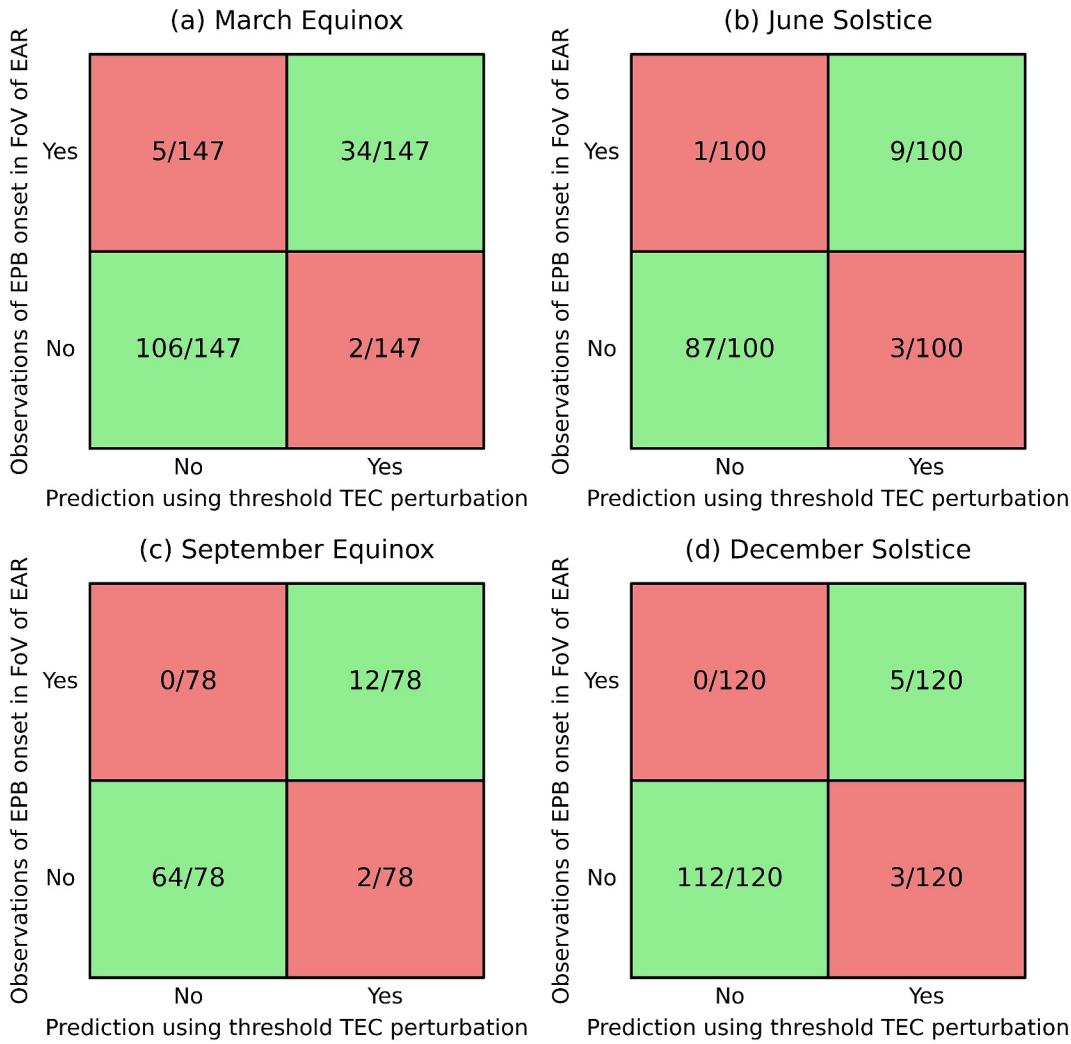


**Figure 10.** Same as Figure 9, but for seasons (a) March equinox, (b) June solstice, (c) September equinox, and (d) December equinox.

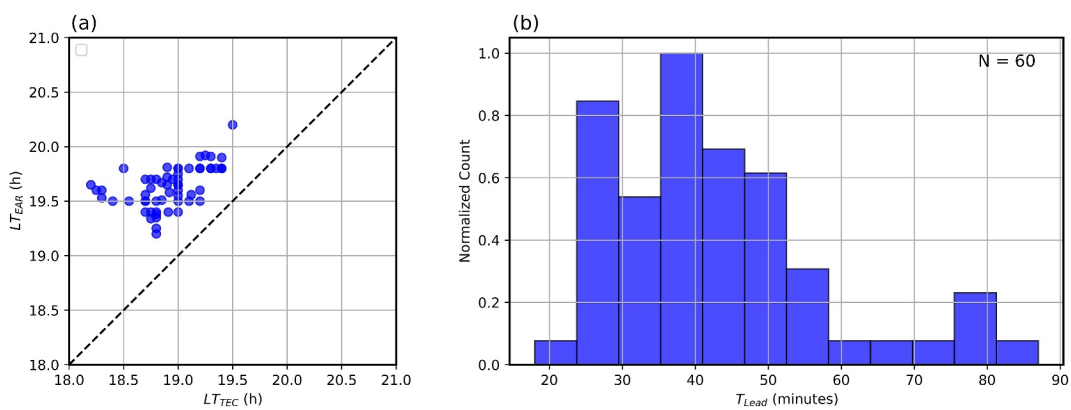


**Figure 11.** (a) Scatter plot between time of detection of threshold TEC perturbation and observation of EPB onset, within the FoV of EAR, and (b) distribution of lead time of prediction (in minutes).

ionosonde station, it is not capable of characterizing the bottomside upwellings at a location slightly away from the ionosonde station (which is clear from the results presented in Section 4.2). Besides, the present analysis from beacon measurements demonstrates the capability of detecting the potential early signatures of localized upwelling using TEC analysis over a wide range of longitude. While the present approach shows a slightly lower success rate of approximately 96.40% compared to 99.86% achieved using observations made using an ionosonde (Patra & Das, 2025), its ability to detect early signatures of potential localized upwellings across a broad longitudinal zone, including regions over oceans where ground-based instruments are absent, underscores its value for comprehensive monitoring and early warning of EPBs on a regional to global scale.

To enable a comparative evaluation of EPB prediction capability based on C/NOFS's beacon measurements, the performance of the statistical IBP model was assessed using the same data set. The model outputs were obtained at hourly intervals from 19 to 24 LT (for EAR longitude) and validated against EPB occurrence inferred from the EAR observations. For example, the IBP prediction at 19 LT was compared with EAR observation during the 19–20 LT interval, and similarly for other local times, accounting for the 1-hr temporal resolution of the model. We also compared the relative performance of the IBP model and TEC perturbation-based predictions using the ROC analysis (not shown here). The IBP model exhibited its best predictive skill at 21 LT, yielding an AUC of 0.76, $G_c$ of ∼0.52, and a H&KSS score of 0.43 at a $T_h$ of 0.22. In comparison, the TEC-based method demonstrated superior performance with an AUC of 0.97, $G_c$ of ∼0.94 and a H&KSS score of 0.88 at a $T_h$ of 5.65% (see Figure 8). While the utility of the IBP model in providing robust climatological forecasts of EPB occurrence has been demonstrated in Stolle et al. (2024), the present results highlight the essential role of localized measurements in forecasting the day-to-day variability in EPB occurrence.

Now, coming to the events where the present approach failed to predict the occurrence of EPBs. There were 10 instances in which TEC perturbation amplitudes indicated a potential onset of EPBs within the EAR's FoV; however, no fresh EPB development were observed. Conversely, in 6 events, fresh EPB onsets were detected within the EAR FoV despite the TEC perturbation amplitude were limited to less than 5.65% (see Figure 9). These failures underscore certain limitations in characterizing localized upwellings based solely on the TEC perturbation analysis derived from the satellite beacon data. A key consideration is the uncertainty involved in estimating VTEC from the slant TEC measured along oblique paths from the C/NOFS satellite to ground-based receivers (e.g., GRBR). VTEC retrieval requires converting STEC using a mapping function that assumes a fixed-altitude thin-shell ionosphere (for the present study at 350 km). This assumption can lead to uncertainty in the estimation of VTEC, especially when the actual electron density peak deviates from the assumed height or when the ionosphere is vertically structured or disturbed. Additionally, due to the elliptical orbit of C/NOFS (∼400–850 km altitude), the geometry of the beacon signal path changes continuously, further complicating the accuracy and consistency of VTEC estimation over time. Furthermore, VTEC represents an integrated quantity along the line of sight and lacks the capability to resolve altitude-specific plasma variations. Consequently, observed enhancements in TEC perturbations may arise not only from vertical plasma upwellings but also from other processes such as horizontal plasma transport (e.g., Foster & Coster, 2007) or the propagation of traveling ionospheric disturbances (TIDs) (e.g., Figueiredo et al., 2023), which may not be directly associated with EPB initiation. This imposes an inherent limitation on the ability of TEC-based analyses to fully capture localized upwelling structures near the bottomside F-region, and such limitations should be carefully considered when interpreting prediction outcomes derived from this method.

In conclusion, this study suggests that the identification of potential localized upwellings using TEC data derived from satellite beacon measurements may provide a means to predict EPB occurrences across a broad longitudinal sector. While this technique may not detect localized upwellings with the same precision as ground-based instruments such as an ionosonde (Patra & Das, 2025), it exhibits comparable performance to existing prediction methods (e.g., Anderson & Redmon, 2017; Carter et al., 2014; Garcia et al., 2023; Jia et al., 2023; Zhao et al., 2021),where prediction of EPBs is typically achieved with accuracies below or equal to 90%. However, for practical implementation, the proposed approach should be validated across different longitudinal sectors to determine region-specific thresholds for characterizing localized upwellings. This is essential because the optimal TEC perturbation threshold may vary depending on the regional EPB occurrence climatology and other influencing factors such as geomagnetic configuration, background ionospheric conditions, and local electrodynamics. Such an investigation will be undertaken in future studies to enhance the robustness and global applicability of the method. It is important to note that the advance prediction time for forecasting EPB occurrence using TEC data strongly depends on the orbital timing of the satellite (e.g., C/NOFS), particularly on the local time at which it

passes over a given longitude sector around sunset. To address this issue, we propose a satellite mission concept involving multiple low-inclination satellites, similar to C/NOFS, traversing the same longitude sector in ∼30 min (preferably between 17:30 and 19:30 LT) intervals during the evening period, and paired with a network of GRBR-like ground receivers. This configuration could enable detailed temporal and spatial characterization of ionospheric upwellings responsible for EPB initiation, enhancing our ability to forecast space weather impacts in the equatorial ionosphere.

## Conflict of Interest

The authors declare no conflicts of interest relevant to this study.

## Data Availability Statement

The TEC data used for the present analysis can be obtained at Das et al. (2025). The EAR data is publicly available at https://www2.rish.kyoto-u.ac.jp/radar-group/ear/data-fai/. The ionosonde data from Chumphon can be obtained at https://wdc.nict.go.jp/Ionosphere/archive/ionog_viewer_fmcw/. The solar-flux (F10.7 cm) and Kp data can be obtained directly from OMNI website at https://omniweb.gsfc.nasa.gov/form/dx1.html.

**Acknowledgments**
SKD thanks the Alexander von Humboldt Foundation for the Humboldt Postdoctoral Research Fellowship. SKD also thanks Dr. S. Tulasi Ram for providing valuable insight on analyzing the GRBR data. This work has also been supported by the International joint research of geosPace variaBility by combining multi-point ground And SatEllite observations and modeling (PBASE program; JSPS KAKENHI Grant 22K21345). The authors greatly acknowledge the Research Institute for Sustainable Humanosphere (RISH) of Kyoto University for the use of EAR radar data. The authors also acknowledge the use of Chumphon ionosonde data, which is a part of the SEALION project under the National Institute of Information and Communications Technology (NICT), Japan. Open Access funding enabled and organized by Projekt DEAL.

## References

Abdu, M. (2001). Outstanding problems in the equatorial ionosphere–thermosphere electrodynamics relevant to spread F. *Journal of Atmospheric and Solar-Terrestrial Physics*, *63*(9), 869–884. https://doi.org/10.1016/S1364-6826(00)00201-7

Aitchison, G., & Weekes, K. (1959). Some deductions of ionospheric information from the observations of emissions from satellite 1957α2—I: The theory of the analysis. *Journal of Atmospheric and Terrestrial Physics*, *14*(3–4), 236–243. https://doi.org/10.1016/0021-9169(59)90035-2

Anderson, D. N., & Redmon, R. J. (2017). Forecasting scintillation activity and equatorial spread F. *Space Weather*, *15*(3), 495–502. https://doi.org/10.1002/2016SW001554

Balsley, B. B., Haerendel, G., & Greenwald, R. A. (1972). Equatorial spread F: Recent observations and a new interpretation. *Journal of Geophysical Research*, *77*(28), 5625–5628. https://doi.org/10.1029/JA077i028p05625

Barnes, G., Leka, K. D., Schrijver, C. J., Colak, T., Qahwaji, R., Ashamari, O. W., et al. (2016). A comparison of flare forecasting methods. I. Results from the "All-Clear" workshop. *The Astrophysical Journal*, *829*(2), 89. https://doi.org/10.3847/0004-637X/829/2/89

Booker, H. G., & Wells, H. W. (1938). Scattering of radio waves by the F-region of the ionosphere. *Terrestrial Magnetism and Atmospheric Electricity*, *43*(3), 249–256. https://doi.org/10.1029/TE043i003p00249

Burke, W. J., Gentile, L. C., Huang, C. Y., Valladares, C. E., & Su, S. Y. (2004). Longitudinal variability of equatorial plasma bubbles observed by DMSP and ROCSAT-1. *Journal of Geophysical Research*, *109*(A12). https://doi.org/10.1029/2004JA010583

Carter, B. A., Yizengaw, E., Retterer, J. M., Francis, M., Terkildsen, M., Marshall, R., et al. (2014). An analysis of the quiet time day-to-day variability in the formation of postsunset equatorial plasma bubbles in the Southeast Asian region. *Journal of Geophysical Research: Space Physics*, *119*(4), 3206–3223. https://doi.org/10.1002/2013JA019570

Clemesha, B., & Wright, R. (1966). A survey of equatorial spread F (Spread-F irregularities, and diurnal, seasonal, and sunspot cycle variations in relation to other ionospheric parameters) (pp. 3–27).

Das, S. K., Janardana Reddy, G., Patra, A. K., & Niranjan, K. (2022). Onset conditions and features of equatorial F region irregularities: New insight from collocated digisonde and radar observations from Gadanki. *Journal of Geophysical Research: Space Physics*, *127*(2), e2021JA029715. https://doi.org/10.1029/2021JA029715

Das, S. K., Patra, A. K., Kherani, E. A., Chaitanya, P. P., & Niranjan, K. (2020). Relationship between presunset wave structures and interbubble spacing: The seeding perspective of equatorial plasma bubble. *Journal of Geophysical Research: Space Physics*, *125*(8), e2020JA028122. https://doi.org/10.1029/2020JA028122

Das, S. K., Patra, A. K., & Niranjan, K. (2021). On the assessment of day-to-day occurrence of equatorial plasma bubble. *Journal of Geophysical Research: Space Physics*, *126*(5), e2021JA029129. https://doi.org/10.1029/2021JA029129

Das, S. K., Pavanchaitanya, P., Patra, A. K., & Niranjan, K. (2022). On the onset time and background ionospheric conditions of postsunset equatorial plasma bubble. *Journal of Geophysical Research: Space Physics*, *127*(12), e2022JA030731. https://doi.org/10.1029/2022JA030731

Das, S. K., Stolle, C., Yamazaki, Y., Yokoyama, T., & Yamamoto, M. (2025). Forecasting equatorial plasma bubbles from precursor TEC signatures observed by C/NOFS [Dataset]. *Zenodo*. https://doi.org/10.5281/zenodo.17120298

Davies, K. (1980). Recent progress in satellite radio beacon studies with particular emphasis on the ATS-6 radio beacon experiment. *Space Science Reviews*, *25*(4), 357–430. https://doi.org/10.1007/BF00241558

de La Beaujardière, O., Jeong, L., Basu, B., Basu, S., Beach, T., Bernhardt, P., et al. (2004). C/NOFS: A mission to forecast scintillations. *Journal of Atmospheric and Solar-Terrestrial Physics*, *66*(17), 1573–1591. https://doi.org/10.1016/j.jastp.2004.07.030

De Michelis, P., Consolini, G., Pignalberi, A., Lovati, G., Pezzopane, M., Tozzi, R., et al. (2022). Ionospheric turbulence: A challenge for GPS loss of lock understanding. *Space Weather*, *20*(7), e2022SW003129. https://doi.org/10.1029/2022SW003129

Eccles, J. V. (1998). Modeling investigation of the evening prereversal enhancement of the zonal electric field in the equatorial ionosphere. *Journal of Geophysical Research*, *103*(A11), 26709–26719. https://doi.org/10.1029/98JA02656

Figueiredo, C. A. O. B., Wrasse, C. M., Vadas, S., Takahashi, H., Otsuka, Y., Nyassor, P. K., et al. (2023). Daytime medium scale traveling ionospheric disturbances (MSTIDS) over the Andes Mountains at equatorial and low magnetic latitudes. *Journal of Geophysical Research: Space Physics*, *128*(10), e2023JA031477. https://doi.org/10.1029/2023JA031477

Foster, J., & Coster, A. (2007). Conjugate localized enhancement of total electron content at low latitudes in the American sector. *Journal of Atmospheric and Solar-Terrestrial Physics*, *69*(10–11), 1241–1252. https://doi.org/10.1016/j.jastp.2006.09.012

Fukao, S., Hashiguchi, H., Yamamoto, M., Tsuda, T., Nakamura, T., Yamamoto, M. K., et al. (2003). Equatorial atmosphere radar (EAR): System description and first results. *Radio Science*, *38*(3). https://doi.org/10.1029/2002RS002767

Garcia, D., Rojas, E. L., & Hysell, D. L. (2023). Predicting equatorial ionospheric convective instability using machine learning. *Space Weather*, *21*(12), e2023SW003505. https://doi.org/10.1029/2023SW003505

Garriott, O. K. (1960). The determination of ionospheric electron content and distribution from satellite observations: 2. Results of the analysis. *Journal of Geophysical Research*, *65*(4), 1151–1157. https://doi.org/10.1029/JZ065i004p01151

Haerendel, G. (1973). Theory of equatorial spread F.

Haerendel, G., Eccles, J. V., & Çakir, S. (1992). Theory for modeling the equatorial evening ionosphere and the origin of the shear in the horizontal plasma flow. *Journal of Geophysical Research*, *97*(A2), 1209–1223. https://doi.org/10.1029/91JA02226

Hanssen, A., & Kuipers, W. (1965). *On the relationship between the frequency of rain and various meteorological parameters. (With reference to the problem of objective forecasting)*. Koninklijk Nederlands Meteorologisch Instituut.

Hedin, A. E. (1991). Extension of the MSIS thermosphere model into the middle and lower atmosphere. *Journal of Geophysical Research*, *96*(A2), 1159–1172. https://doi.org/10.1029/90ja02125

Huang, C.-S., & Hairston, M. R. (2015). The postsunset vertical plasma drift and its effects on the generation of equatorial plasma bubbles observed by the C/NOFS satellite. *Journal of Geophysical Research: Space Physics*, *120*(3), 2263–2275. https://doi.org/10.1002/2014JA020735

Huang, C.-S., & Kelley, M. C. (1996). Nonlinear evolution of equatorial spread F: 2. Gravity wave seeding of Rayleigh-Taylor instability. *Journal of Geophysical Research*, *101*(A1), 293–302. https://doi.org/10.1029/95JA02210

Hysell, D. L., Milla, M. A., & Kuyeng, K. (2019). Radio beacon and radar assessment and forecasting of equatorial F region ionospheric stability. *Journal of Geophysical Research: Space Physics*, *124*(11), 9511–9524. https://doi.org/10.1029/2019JA026991

Jia, G., Luo, W., Yu, X., Zhu, Z., & Chang, S. (2023). Determining the day-to-day occurrence of low-latitude scintillation in equinoxes at Sanya during high solar activities (2012–2013). *Atmosphere*, *14*(8), 1242. https://doi.org/10.3390/atmos14081242

Jolliffe, I. T., & Stephenson, D. B. (2011). *Forecast verification: A practitioner's guide in atmospheric science*. John Wiley & Sons.

Kelley, M. C. (2009). *The Earth's ionosphere: Plasma physics and electrodynamics* (Vol. 96). Academic Press.

Kelley, M. C., Haerendel, G., Kappler, H., Valenzuela, A., Balsley, B. B., Carter, D. A., et al. (1976). Evidence for a Rayleigh-Taylor type instability and upwelling of depleted density regions during equatorial spread F. *Geophysical Research Letters*, *3*(8), 448–450. https://doi.org/10.1029/GL003i008p00448

Kelley, M. C., Larsen, M. F., LaHoz, C., & McClure, J. P. (1981). Gravity wave initiation of equatorial spread F: A case study. *Journal of Geophysical Research*, *86*(A11), 9087–9100. https://doi.org/10.1029/JA086iA11p09087

Kintner, P. M., Ledvina, B. M., & de Paula, E. R. (2007). GPS and ionospheric scintillations. *Space Weather*, *5*(9). https://doi.org/10.1029/2006SW000260

Leitinger, R., Schmidt, G., & Tauriainen, A. (1975). An evaluation method combining the differential Doppler measurements from two stations that enables the calculation of the electron content of the ionosphere. *Journal of Geophysics*, *41*(1), 201–213. https://n2t.net/ark:/88439/y034043

Makela, J. J., Vadas, S. L., Muryanto, R., Duly, T., & Crowley, G. (2010). Periodic spacing between consecutive equatorial plasma bubbles. *Geophysical Research Letters*, *37*(14). https://doi.org/10.1029/2010GL043968

Maruyama, T., Kawamura, M., Saito, S., Nozaki, K., Kato, H., Hemmakorn, N., et al. (2007). Low latitude ionosphere-thermosphere dynamics studies with inosonde chain in Southeast Asia. *Annales Geophysicae*, *25*(7), 1569–1577. https://doi.org/10.5194/angeo-25-1569-2007

Mason, I. (1982). A model for assessment of weather forecasts. *Australian Meteorological Magazine*, *30*, 291–303.

Matzka, J., Stolle, C., Yamazaki, Y., Bronkalla, O., & Morschhauser, A. (2021). The geomagnetic Kp index and derived indices of geomagnetic activity. *Space Weather*, *19*(5), e2020SW002641. https://doi.org/10.1029/2020SW002641

Murray, S. A., Bingham, S., Sharpe, M., & Jackson, D. R. (2017). Flare forecasting at the met office space weather operations centre. *Space Weather*, *15*(4), 577–588. https://doi.org/10.1002/2016SW001579

Narayanan, V. L., Sau, S., Gurubaran, S., Shiokawa, K., Balan, N., Emperumal, K., & Sripathi, S. (2014). A statistical study of satellite traces and evolution of equatorial spread F. *Earth Planets and Space*, *66*, 1–13. https://doi.org/10.1186/s40623-014-0160-4

Nishizuka, N., Kubo, Y., Sugiura, K., Den, M., & Ishii, M. (2020). Reliable probability forecast of solar flares: Deep flare net-reliable (DeFN-R). *The Astrophysical Journal*, *899*(2), 150. https://doi.org/10.3847/1538-4357/aba2f2

Ott, E. (1978). Theory of Rayleigh-Taylor bubbles in the equatorial ionosphere. *Journal of Geophysical Research*, *83*(A5), 2066–2070. https://doi.org/10.1029/JA083iA05p02066

Patra, A. K., Ajith, K. K., & Perwitasari, S. (2025). On the short-range longitudinal variation of pre-reversal enhancement of vertical plasma drift and associated implications. *Journal of Geophysical Research: Space Physics*, *130*(3), e2024JA033124. https://doi.org/10.1029/2024JA033124

Patra, A. K., & Das, S. K. (2023). On the upwelling of the F layer base and prediction of equatorial plasma bubble. *Geophysical Research Letters*, *50*(7), e2023GL102803. https://doi.org/10.1029/2023GL102803

Patra, A. K., & Das, S. K. (2025). Prediction of equatorial plasma bubble formation using ionosonde observations from India. *AGU Advances*, *6*(1), e2024AV001323. https://doi.org/10.1029/2024AV001323

Patra, A. K., Srinivasulu, P., Chaitanya, P. P., Rao, M. D., & Jayaraman, A. (2014). First results on low-latitude E and F region irregularities obtained using the Gadanki Ionospheric Radar Interferometer. *Journal of Geophysical Research: Space Physics*, *119*(12), 10276–10293. https://doi.org/10.1002/2014JA020604

Reddy, S. A., Forsyth, C., Aruliah, A., Smith, A., Bortnik, J., Aa, E., et al. (2023). Predicting swarm equatorial plasma bubbles via machine learning and Shapley values. *Journal of Geophysical Research: Space Physics*, *128*(6), e2022JA031183. https://doi.org/10.1029/2022JA031183

Redmon, R. J., Anderson, D., Caton, R., & Bullett, T. (2010). A forecasting ionospheric real-time scintillation tool (FIRST). *Space Weather*, *8*(12). https://doi.org/10.1029/2010SW000582

Röttger, J. (1973). Wave-like structures of large-scale equatorial spread-F irregularities. *Journal of Atmospheric and Terrestrial Physics*, *35*(6), 1195–1206. https://doi.org/10.1016/0021-9169(73)90016-0

Scannapieco, A. J., & Ossakow, S. L. (1976). Nonlinear equatorial spread F. *Geophysical Research Letters*, *3*(8), 451–454. https://doi.org/10.1029/GL003i008p00451

Shinagawa, H., Jin, H., Miyoshi, Y., Fujiwara, H., Yokoyama, T., & Otsuka, Y. (2018). Daily and seasonal variations in the linear growth rate of the Rayleigh-Taylor instability in the ionosphere obtained with GAIA. *Progress in Earth and Planetary Science*, *5*(1), 16. https://doi.org/10.1186/s40645-018-0175-8

Singh, S., Johnson, F. S., & Power, R. A. (1997). Gravity wave seeding of equatorial plasma bubbles. *Journal of Geophysical Research*, *102*(A4), 7399–7410. https://doi.org/10.1029/96JA03998

Stolle, C., Siddiqui, T. A., Schreiter, L., Das, S. K., Rusch, I., Rother, M., & Doornbos, E. (2024). An empirical model of the occurrence rate of low latitude post-sunset plasma irregularities derived from CHAMP and swarm magnetic observations. *Space Weather*, *22*(6), e2023SW003809. https://doi.org/10.1029/2023SW003809

Sultan, P. J. (1996). Linear theory and modeling of the Rayleigh-Taylor instability leading to the occurrence of equatorial spread F. *Journal of Geophysical Research*, *101*(A12), 26875–26891. https://doi.org/10.1029/96JA00682

Swets, J. A. (1973). The relative operating characteristic in psychology: A technique for isolating effects of response bias finds wide use in the study of perception and cognition. *Science*, *182*(4116), 990–1000. https://doi.org/10.1126/science.182.4116.990

Takahashi, H., Taylor, M. J., Pautet, P. D., Medeiros, A. F., Gobbi, D., Wrasse, C. M., et al. (2008). Simultaneous observation of ionospheric plasma bubbles and mesospheric gravity waves during the SpreadFEx campaign. *Annales Geophysicae*, *27*(4), 1477–1487. https://doi.org/10.5194/angeo-27-1477-2009

Tapping, K. F. (2013). The 10.7cm solar radio flux (F10.7). *Space Weather*, *11*(7), 394–406. https://doi.org/10.1002/swe.20064

Thampi, S. V., Yamamoto, M., Tsunoda, R. T., Otsuka, Y., Tsugawa, T., Uemoto, J., & Ishii, M. (2009). First observations of large-scale wave structure and equatorial spread F using CERTO radio beacon on the C/NOFS satellite. *Geophysical Research Letters*, *36*(18). https://doi.org/10.1029/2009GL039887

Tsunoda, R. T. (1983). On the generation and growth of equatorial backscatter plumes: 2. Structuring of the west walls of upwellings. *Journal of Geophysical Research*, *88*(A6), 4869–4874. https://doi.org/10.1029/JA088iA06p04869

Tsunoda, R. T. (1985). Control of the seasonal and longitudinal occurrence of equatorial scintillations by the longitudinal gradient in integrated E region Pedersen conductivity. *Journal of Geophysical Research*, *90*(A1), 447–456. https://doi.org/10.1029/JA090iA01p00447

Tsunoda, R. T. (2005). On the enigma of day-to-day variability in equatorial spread F. *Geophysical Research Letters*, *32*(8). https://doi.org/10.1029/2005GL022512

Tsunoda, R. T. (2008). Satellite traces: An ionogram signature for large-scale wave structure and a precursor for equatorial spread F. *Geophysical Research Letters*, *35*(20). https://doi.org/10.1029/2008GL035706

Tsunoda, R. T. (2015). Upwelling: A unit of disturbance in equatorial spread F. *Progress in Earth and Planetary Science*, *2*, 1–14. https://doi.org/10.1186/s40645-015-0038-5

Tsunoda, R. T., Baron, M. J., Owen, J., & Towle, D. M. (1979). ALTAIR: An incoherent scatter radar for equatorial spread F studies. *Radio Science*, *14*(6), 1111–1119. https://doi.org/10.1029/RS014i006p01111

Tsunoda, R. T., & Ecklund, W. L. (2007). On the post-sunset rise of the equatorial F layer and superposed upwellings and bubbles. *Geophysical Research Letters*, *34*(4). https://doi.org/10.1029/2006GL028832

Tsunoda, R. T., Livingston, R. C., McClure, J. P., & Hanson, W. B. (1982). Equatorial plasma bubbles: Vertically elongated wedges from the bottomside F layer. *Journal of Geophysical Research*, *87*(A11), 9171–9180. https://doi.org/10.1029/JA087iA11p09171

Tsunoda, R. T., Thampi, S. V., Nguyen, T. T., & Yamamoto, M. (2013). On validating the relationship of ionogram signatures to large-scale wave structure. *Journal of Atmospheric and Solar-Terrestrial Physics*, *103*, 30–35. https://doi.org/10.1016/j.jastp.2012.11.003

Tsunoda, R. T., & White, B. R. (1981). On the generation and growth of equatorial backscatter plumes 1. Wave structure in the bottomside F layer. *Journal of Geophysical Research*, *86*(A5), 3610–3616. https://doi.org/10.1029/JA086iA05p03610

Tsunoda, R. T., Yamamoto, M., Tsugawa, T., Hoang, T. L., Tulasi Ram, S., Thampi, S. V., et al. (2011). On seeding, large-scale wave structure, equatorial spread F, and scintillations over Vietnam. *Geophysical Research Letters*, *38*(20). https://doi.org/10.1029/2011GL049173

Tulasi Ram, S., Yamamoto, M., Tsunoda, R. T., Chau, H. D., Hoang, T. L., Damtie, B., et al. (2014). Characteristics of large-scale wave structure observed from African and Southeast Asian longitudinal sectors. *Journal of Geophysical Research: Space Physics*, *119*(3), 2288–2297. https://doi.org/10.1002/2013JA019712

Tulasi Ram, S., Yamamoto, M., Tsunoda, R. T., Thampi, S. V., & Gurubaran, S. (2012). On the application of differential phase measurements to study the zonal large scale wave structure (LSWS) in the ionospheric electron content. *Radio Science*, *47*(2). https://doi.org/10.1029/2011RS004870

Weber, E. J., Buchau, J., Eather, R. H., & Mende, S. B. (1978). North-south aligned equatorial airglow depletions. *Journal of Geophysical Research*, *83*(A2), 712–716. https://doi.org/10.1029/JA083iA02p00712

Woodman, R. F., & La Hoz, C. (1976). Radar observations of F region equatorial irregularities. *Journal of Geophysical Research*, *81*(31), 5447–5466. https://doi.org/10.1029/JA081i031p05447

Xiong, C., Stolle, C., & Lühr, H. (2016). The Swarm satellite loss of GPS signal and its relation to ionospheric plasma irregularities. *Space Weather*, *14*(8), 563–577. https://doi.org/10.1002/2016SW001439

Yamamoto, M. (2008). Digital beacon receiver for ionospheric TEC measurement developed with GNU Radio. *Earth Planets and Space*, *60*(11), e21–e24. https://doi.org/10.1186/BF03353137

Yokoyama, T., Fukao, S., & Yamamoto, M. (2004). Relationship of the onset of equatorial F region irregularities with the sunset terminator observed with the equatorial atmosphere radar. *Geophysical Research Letters*, *31*(24). https://doi.org/10.1029/2004GL021529

Zhao, X., Li, G., Xie, H., Hu, L., Sun, W., Yang, S., et al. (2021). The prediction of day-to-day occurrence of low latitude ionospheric strong scintillation using gradient boosting algorithm. *Space Weather*, *19*(12), e2021SW002884. https://doi.org/10.1029/2021SW002884